Structural and mechanistic insight into ribosomal ITS2 RNA processing by nuclease-kinase machinery

Jiyun Chen,[1,†] Hong Chen,[1,†] Shanshan Li,[2,†] Xiaofeng Lin,[1] Rong Hu,[1] Kaiming Zhang,[2,*] and Liang Liu[1,*]

[1] State Key Laboratory of Cellular Stress Biology, School of Life Sciences, Faculty of Medicine and Life Sciences, Xiamen University, Xiamen 361102, China and [2] MOE Key Laboratory for Cellular Dynamics and Division of Life Sciences and Medicine, University of Science and Technology of China, Hefei 230027, China

*For correspondence: kmzhang@ustc.edu.cn (K.Z.); liangliu2019@xmu.edu.cn (L.L.)

[†]These authors contributed equally to this work.

Abstract

Precursor ribosomal RNA (pre-rRNA) processing is a key step in ribosome biosynthesis and involves numerous RNases. A HEPN nuclease Las1 and a polynucleotide kinase Grc3 assemble into a tetramerase responsible for rRNA maturation. Here, we report the structures of full-length *Saccharomyces cerevisiae* and *Cyberlindnera jadinii* Las1-Grc3 complexes, and *Cyberlindnera jadinii* Las1. The Las1-Grc3 structures show that the central coiled coil domain of Las1 facilitates pre-rRNA binding and cleavage, while the Grc3 C-terminal loop motif directly binds to the HEPN active center of Las1 and regulates pre-rRNA cleavage. Structural comparison between Las1 and Las1-Grc3 complex exhibits that Grc3 binding induces conformational rearrangements of catalytic residues associated with HEPN nuclease activation. Biochemical assays identify that Las1 processes pre-rRNA at the two specific sites (C2 and C2′), which greatly facilitates rRNA maturation. Our structures and specific pre-rRNA cleavage findings provide crucial insights into the mechanism and pathway of pre-rRNA processing in ribosome biosynthesis.

Introduction

Ribosomes are large molecular machines assembled from numerous proteins and RNAs that are responsible for protein synthesis in cells (Anger et al., 2013; Gasse, Flemming, & Hurt, 2015; Khatter, Myasnikov, Natchiar, & Klaholz, 2015). In eukaryotes, ribosome biosynthesis is tightly coupled to cell growth and cell cycle progression and is critical for regulating normal cell size and maintaining cell cycle progression (Castle et al., 2013). Ribosome biosynthesis is an extremely complicated process involving about 200 assembly and processing factors, which are involved in a series of continuous assembly and processing reactions such as ribosome protein folding, modification, assembly, and precursor rRNA (pre-rRNA) processing (Gasse et al., 2015; Lafontaine, 2015; Pillon, Sobhany, Borgnia, Williams, & Stanley, 2017; Wu et al., 2016). Mature ribosomes in yeast *Saccharomyces cerevisiae* contain 79 proteins and four RNAs (25S, 18S, 5.8S, and 5S rRNA) (Doudna & Rath, 2002; Wilson & Doudna Cate, 2012; Woolford & Baserga, 2013). 5S rRNA is transcribed by RNA polymerase III, whereas 25S, 18S and 5.8S rRNA are cotranscribed by RNA polymerase I as a single long precursor (35S pre-rRNA) (Tomecki, Sikorski, & Zakrzewska-Placzek, 2017). Except 25S, 18S and 5.8S rRNA sequences, the 35S pre-rRNA also includes 5′-external transcribed spacer sequence (ETS), 3′-external transcribed spacer sequence, and two internal transcribed spacer sequences (ITS1 and ITS2) (Fromm et al., 2017). ITS1 located between 5.8S and 18S rRNA and ITS2 located between 5.8S and 25S rRNA (Coleman, 2003; Cote, Greer, & Peculis, 2002). The mature rRNAs are generated by a large number of endonucleases and exonucleases that remove these transcribed spacers step by step through multiple efficient and correct processing reactions (Granneman, Petfalski, & Tollervey, 2011). The pre-rRNA processing factors synergistically produce mature rRNAs and lead to an accurate and efficient assembly of mature ribosome in the nucleolus, which

are key to cell survival (Pillon & Stanley, 2018). Mutations in the genes that encode these pre-rRNA processing factors are often lethal (Tomecki et al., 2017). Although numerous evolutionarily conserved protein factors have been found to be involved in the processing and modification of ribosomal RNA, the detailed pathways of these factors and their specific processing mechanisms are not well understood.

Las1 and Grc3 are highly conserved proteins and have recently been identified as core enzymes involved in processing and removing ITS2 spacer, which is a key step in the synthesis of 60S ribosomal subunit (Gasse et al., 2015; Schillewaert, Wacheul, Lhomme, & Lafontaine, 2012). Las1 is characterized as a nucleolar protein essential for ribosome biogenesis, as well as cell proliferation and cell viability in *Saccharomyces cerevisiae* (Castle, Cassimere, & Denicourt, 2012; Castle, Cassimere, Lee, & Denicourt, 2010; Doseff & Arndt, 1995). It is important to determine the role of Las1 in rRNA metabolic pathways and regulatory networks associated with ribosome biogenesis and cell proliferation. Recent studies have demonstrated that Las1 is an endoribonuclease that contains a HEPN (higher eukaryote and prokaryote nucleotide binding) domain responsible for rRNA processing (Pillon et al., 2020; Pillon et al., 2017). The HEPN domain must be dimerized to form an active nuclease, such as the Cas13 effectors in CRISPR immune defense systems, whose catalytic site is formed by two HEPN domains involved in non-specific cleavage of single-stranded RNA (Knott et al., 2017; Liu, Li, Ma, et al., 2017; Liu, Li, Wang, et al., 2017; Zhang et al., 2018). Interestingly, Las1 specifically cleaves at the C2 site within ITS2 and generates the 7S pre-rRNA and 26S pre-rRNA (Fernandez-Pevida, Kressler, & de la Cruz, 2015). It is not clear why Las1 HEPN nuclease specifically targets and cleaves ITS2 only at C2 site, and whether this cleavage depends on a specific sequence or secondary structure. In addition, the cleavage activity of Las1 is primarily

dependent on another enzyme Grc3. Grc3 is a polynucleotide kinase responsible not only for Las1 nuclease activation, but also for nonspecific phosphorylation of the 5′-OH of the 26S pre-rRNA produced by Las1 cleavage, providing a signal for further processing by Rat1-Rai1 exonuclease (Gordon, Pillon, & Stanley, 2019; Xiang et al., 2009). Although Cryo-EM reveals cross-linked *Chaetomium thermophilum* (Ct) Las1 and Grc3 assemble into a super-dimer, due to flexibility, critical structural information is missing for the coiled coil (CC) domain of Las1 and the N-terminal and C-terminal regions of Grc3 (Pillon et al., 2019). It remains unknown how Las1 and Grc3 coordinate with each other in terms of substrate binding and nuclease activation.

In this study, we identified that *S. cerevisiae* (Sc) Las1 endoribonuclease initially cleaves ITS2 in a step-by-step fashion at two specific sites, which greatly promotes the maturation of 25S rRNA. Additionally, we solved the crystal structures of full-length ScLas1-Grc3 complex and *Cyberlindnera jadinii* (Cj) Las1-Grc3 complex, as well as the high resolution structure of CjLas1 HEPN domain. Our structural and biochemical findings uncovered a detailed mechanism of polynucleotide kinase-mediated activation of HEPN nuclease, providing a molecular basis for clearly understanding the process of pre-rRNA processing and maturation in ribosome biosynthesis.

Results

Las1 cleaves ITS2 at two specific sites

HEPN endoribonucleases such as Cas13, Ire1, and RNase L are metal-independent RNA specific enzymes that efficiently cleave substrate RNA at multiple sites (Abudayyeh et al., 2016; Huang et al., 2014; Korennykh et al., 2009; Lee et al., 2008; Wang et al., 2014). Las1 is also identified as a HEPN-containing RNase, but it has only been found to initially cut ITS2 RNA at a single specific position (C2). To investigate whether there are other potential

sites for Las1 cleavage in ITS2, we performed *in vitro* RNA cleavage assays using a 5′-Cy5- and 3′-Cy3-labeled 33-nt ITS2 RNA substrate (Figure 1A). Las1 shows weak or no detectable activity to ITS2 in the absence of Grc3, but exhibits robust activity in the presence of Grc3 (Figure 1B, Figure 1–figure supplement 1), revealing Grc3-dependent Las1 nuclease activation. Interesting, we observed a single 5′-Cy5-labeled cleavage product, and two prominent 3′-Cy3-labeled cleavage products including a final product and an intermediate product (Figure 1B), suggesting that cleavage of ITS2 substrate occurs at two specific sites. The 33-nt ITS2 substrate RNA harbors the C2 site, which is located between nucleotides A140 and G141 (Figure 1A). In addition to the C2 site, there is another specific position in ITS2 that is able to be processed by Las1. ScLas1 cleaves the 33-nt ITS2 at C2 site to theoretically generate a 10-nt 5′-terminal product and a 23-nt 3′-terminal product (Figure 1A). Our merger data shows that the final 5′-terminal and 3′-terminal product bands are at nearly the same horizontal position on the gel (Figure 1B), indicating that they are very close in length. Therefore, we hypothesize that the 23-nt 3′-terminal product is an intermediate that can be further processed by Las1 at a specific site to produce two small products. We then mapped the cleavage products using the 33-nt ITS2 RNA without 5′-Cy5- and 3′-Cy3-label. We observed four cleavage bands, two approximately 23-nt (P2) and 14-nt (P3) in length, and two (P1 and P4) less than 11-nt in length (Figure 1C). The 23-nt product (P2) is obviously an intermediate cleavage product, which is further cleaved to generate 14-nt and 9-nt products. Based on these observations, we identify that another cleavage site, which we designated as C2′, is located between nucleotides G154 and C155. Las1 is able to process ITS2 at C2 and C2′ sites in a step-by-step manner, resulting in a 9-nt 3′-end product and a 10-nt 5′-end product.

We obtained similar cleavage results with a longer 81-nt ITS2 RNA substrate

(Figure 1D, E). To further confirm the cleavage site of C2′, we then mapped the cleavage sites of the 81-nt ITS2 using reverse transcription coupling sequencing methods (Figure 1F). We used an adaptor RNA to separately link the product RNA fragments to form template RNAs. After reverse transcription and sequencing of these template RNAs, we obtained the accurate sequence information for products P2 and P4, revealing that the C2 site is located between nucleotides A140 and G141, and the C2′ site is located between nucleotides G154 and C155.

The cleavage products P2, P3, and P4 are all phosphorylated by Grc3, as they all show a slight shift when in the presence of ATP in the reaction (Figure 1G). This indicates that Las1 generates 5′-OH terminus following both C2 and C2′ cleavage. The phosphorylated products are further degraded by Rat1-Rai1 exonuclease, especially P2 and P4, which are completely degraded under given experimental conditions (Figure 1H). P3 is likely too short to degrade completely.

In addition, Grc3 shows no cleavage activity to ITS2 (Figure 1–figure supplement 2), and mutations in the HEPN catalytic residues of Las1 abolish C2 and C2′ cleavage (Figure 1–figure supplement 3), further confirming that both C2 and C2′ cleavages are attributed to metal-independent Las1 RNase (Figure 1–figure supplement 4).

Overall structures of ScLas1-Grc3 complex and CjLas1-Grc3 complex

To elucidate how Las1 and Grc3 cooperate to direct ITS2 cleavage and phosphorylation, we determined the cryo-electron microscopy (cryo-EM) and crystal structures of full-length ScLas1-Grc3 complex at 3.07 Å and 3.69 Å resolution (Figure 2, Figure 2–figure supplement 1, Table 1 and Table 2), respectively. Cleavage assay indicates that ScGrc3 can activate ScLas1

nuclease well for ITS2 cleavage, while CjGrc3 exhibits relatively weak activation ability for CjLas1 nuclease (Figure 1B, Figure 1–figure supplement 1). To better understand the differences in the mechanisms of Grc3 activation of Las1 between different species, we also solved the cryo-EM and crystal structures of full-length CjLas1-Grc3 complex at 3.39 Å and 3.39 Å resolution (Figure 3, Figure 3–figure supplement 1, Table 1 and Table 2), respectively. To be noted, the crystal structures were solved by molecular replacement method with the cryo-EM maps of Las1-Grc3 complexes. Since the crystal structures have similar quality and resolve more structural information than the cryo-EM structures (Figure 3–figure supplement 2), the subsequent presentations and descriptions are based more on the crystal structures.

Both structures reveal that Las1 and Grc3 assemble into a tetramer with two copies of each (Figure 2B, C and Figure 3B, C). In the tetramer, one Las1 and Grc3 molecules form a C2 symmetry with another Las1 and Grc3 molecules. Las1 consists of a relatively conserved N-terminal HEPN domain, a poorly conserved central coiled coil (CC) domain, and a short C-terminal tail motif (LCT) (Figure 2A, Figure 3A, Figure 3–figure supplement 3). Grc3 is composed of an N-terminal domain (NTD), a central polynucleotide kinase (PNK) domain, a C-terminal domain (CTD), and a short C-terminal loop motif (GCT). A CC domain of Las1 and a copy of Grc3 are assembled into an architecture similar to one wing of a butterfly. The NTD and PNK domains of Grc3 constitute the forewing, while the CTD domain of Grc3 and the CC domain of Las1 form the hindwing. All domains are perfectly stacked together to build a compact and stable tetramer architecture (Figure 2C and Figure 3C). Two HEPN domains from two Las1 copies are tightly symmetrically stacked together to form a HEPN dimer. Two Grc3 molecules are assembled on both sides of Las1 HEPN domains to stabilize the conformation of HEPN dimer. The CC domain is located on one side of Grc3 and forms a sandwich-shaped structure with the

Grc3 and HEPN domains (Figure 2B and Figure 3B), resulting in Grc3 being anchored by the CC and HEPN domains. In addition, the CTD of Grc3 and the HEPN domain of Las1 tightly grasp Las1 LCT and Grc3 GCT, respectively, making Las1-Grc3 tetramer assembly more stable.

Las1 CC domain contributes to ITS2 binding and enhances cutting

In order to explore whether there are structural differences between ScLas1-Grc3 and CjLas1-Grc3 complexes, we conducted structural comparison by superposition the structures of the two complexes. Structural superposition shows that the conformations of all Grc3 domains and Las1 HEPN domains are almost identical in the two complexes, while the conformations of Las1 CC domains are significantly different (Figure 4A).

Dali server reveals that CC domain shares little structural similarity with any known proteins (Holm & Rosenstrom, 2010). CC domain is mainly composed of α helices and is the largest domain of Las1 (Figure 4B), with low sequence similarity among different species (Figure 3–figure supplement 3), yet its function remains unknown. To determine whether it plays a role in Las1 catalyzing ITS2 cleavage, we performed EMSA and *in vitro* RNA cleavage assays using Las1 proteins with or without CC domain truncations. Our data shows that the CC domain contributes to the binding of ITS2 RNA and then facilitates ITS2 cleavage (Figure 4C, D), suggesting that the CC domain may play a role of ITS2 stabilization in the Las1 cutting reaction.

Grc3 GCT binds to the HEPN active center and mediates Las1 activation

The ScLas1-Grc3 tetramer structure shows that two Grc3 GCT are stabilized by two HEPN domains of Las1 (Figure 2). Each Grc3 GCT binds to a groove in each Las1 HEPN domain and extends to the ribonuclease active center (Figure 5A and Figure 5–figure supplement 1), which is formed by the two

HEPN domains via dimerization. Both the crystal and cryo-EM structures shows that the conserved catalytic residues Arg129, His130, His134 with two copies from two HEPN domains form a symmetric catalytic active pocket (Figure 5B and Figure 5–figure supplement 2). The two C-terminals of Grc3 GCTs tightly bind to the catalytic active pocket through packing and hydrogen bond interactions (Figure 5–figure supplement 3). Specifically, the side chain of Trp617 within Grc3 GCT inserts into the active pocket and forms packing and hydrogen bond with catalytic residue His134 (Figure 5B). Moreover, Trp617 and His615 in Grc3 form extensive hydrogen bond with residues Arg136, Leu99, Gly98 and His54 within Las1. The Trp617 residue is highly conserved in Grc3 (Figure 5C), and its mutation completely abolishes the ITS2 cleavage (Figure 5D), but has little effect on Las1 binding (Figure 5E), revealing that it plays a crucial role in the activation of HEPN endonuclease. We also mutated each of the residues at the C-terminal of Grc3 and examined the nuclease activity of Las1 complexes with these mutants. Our data shows that alanine substitution of multiply conserved residues dramatically reduces the ITS2 cleavage (Figure 5F, Figure 5—figure supplement 4), indicating that these residues are also essential for coordinating Las1 HEPN endonuclease activation.

Las1 LCT drives Las1-Grc3 complex assembly

Our crystal and cryo-EM structures exhibit that the Las1 LCT is located in a groove in the CTD domain of Grc3 (Figure 6A, Figure 6-figure supplement 1). Structure analysis reveals that the Las1 LCT is stabilized by the Grc3 CTD through extensive hydrophobic interactions and hydrogen bonding. The side chains of Trp488, Trp494 and Phe499 of Las1 LCT are inserted into the three hydrophobic core regions of Grc3 CTD and form stable hydrophobic interactions with multiple hydrophobic residues of Grc3 (Figure 6B, C and Figure 6-figure supplement 1). Additionally, the side chain of Asn487 and the

main chains of Lys497 and Ser489 of Las1 LCT form multiple hydrogen bonds with the sides of Trp573, His543 and the main side of Gln468 of Grc3 (Figure 6B, C and Figure 6-figure supplement 1). Mutations and deletions of Las1 LCT reduce the enzyme activity of Las1 (Figure 6—figure supplement 2). LCT deletions also significantly affect the association between Las1 and Grc3 (Figure 6—figure supplement 3). These results highlight the functional significance of the sequence-dependent recognition of Las1 LCT by Grc3 CTD.

Special crystal structure of Las1 HEPN domain

The biochemical data shows that Las1 exhibits very weak ability to cut ITS2 RNA at both C2 and C2′ sites in the absence of Grc3 (Figure 1B, Figure 1—figure supplement 1), suggesting that Las1 may exist in a low-activity conformation state prior to assembly with Grc3 (Pillon et al., 2017). To determine the structure of Las1 in the low-activity conformation, we screened about 1200 crystallization conditions with full-length Las1 proteins. Unfortunately, we did not obtain any crystals. We conjectured that the CC domain of Las1 might have a flexible conformation in the absence of Grc3, and then attempted to crystallize Las1 truncated by the CC domain and LCT. After screening a large number of crystallization conditions, we successfully obtained well-ordered crystals of the CjLas1 HEPN domain and determined its structure at 1.80 Å resolution using molecular replacement method (Figure 7A and Table 1).

The crystallographic asymmetric unit contained three Las1 HEPN molecules (HEPN1, HEPN2 and HEPN3), each of which assumes an all α-helical fold (Figure 7A). Analysis of crystal packing and interactions across HEPN-HEPN interfaces suggests that the biological unit of Las1 HEPN domain may contain a homodimer and a monomer. HEPN1 and HEPN2 molecules form a face to

face dimer related through the preudo-2-fold axis, similar to the HEPN dimer in the Las1-Grc3 tetramer structure. Most notably, the molecule HEPN3 is likely not to form a dimer similar to HEPN1-HEPN2 with its symmetry-related molecule. Firstly, the structural superposition of HEPN3 and its symmetry-related molecule with the HEPN1-HEPN2 dimer shows that HEPN1 and HEPN3 molecules superimpose well with core root mean-square deviation (RMSD) of 0.7 Å for 133 Cα atoms, while HEPN2 and symmetry-related HEPN3 molecule exhibit significantly different conformations (Figure 7—figure supplement 1). Secondly, the catalytic residues in HEPN1 and HEPN2 domains are close to each other to form a compact active center, whereas the catalytic residues in HEPN3 and its symmetry-related molecule remain far apart, presenting two separate catalytic sites (Figure 7B, C). These observations suggest that the HEPN3 molecule in the asymmetric unit is probably to be a monomer, which forms a special packing with the dimer of HEPN1-HEPN2 in the crystal.

Together, these results indicate a monomer-dimer equilibrium in the Las1 HEPN domain, which is consistent with the previously reported SEC-MALS data (Pillon et al., 2017).

Conformational changes in Las1 HEPN domain upon Grc3 binding

Since Grc3 binding significantly activates the endonuclease activity of Las1, the HEPN nuclease domains are probably to undergo conformational changes before and after Grc3 binding. We compared the HEPN domain dimer structures in CjLas1 and CjLas1-Grc3 complex by superposition and observed that significant conformational changes occur in HEPN domains upon Grc3 binding (Figure 7D). The conformational change is ~3-4 Å Cα RMSD across all ~150 residues in the domain (~90 residues forming a stable core that only changes by ~1 Å). There is also a shift in the associated HEPN domain in

Las1B domain compared to the bound HEPN in the Las1-Grc3 complex, as shown in Figure 7D: ~1 Å shift and ~12 degree rotation. In order to investigate whether conformational changes occurred in the catalytic center, we further compared the catalytic pocket within the HEPN domains of the two structures. Remarkably, Large conformational changes are observed in the catalytic pocket (Figure 7D). In the Grc3-free Las1 structure, the catalytic residues Arg129, His130 and His134 within one HEPN domain are far from the catalytic residues in the other HEPN domain, while in the Grc3-bound structure, the catalytic residues within two HEPN domains are close to each other (Figure 7D, Figure 7—figure supplement 2). These observations indicate that the Grc3 binding not only stabilizes the Las1 HEPN dimer, but also promotes the formation of a more compact catalytic pocket, showing better catalytic activity for specific cleavage of ITS2. Notably, compared with CjGrc3-bound CjLas1, ScGrc3-bound ScLas1 has a more compact catalytic pocket (Figure 7D, Figure 7—figure supplement 2), which may explain why ScLas1 shows better ITS2 cleavage activity than CjLas1 in the presence of Grc3 (Figure 1B, Figure 1—figure supplement 1). In addition, His130 in the ScLas1-Grc3 complex active site and the analogous His130 in the CjLas1-Grc3 complex active site adopt two different conformations (Figure 7—figure supplement 3), which similar to the conformations of His142 of CtGrc3 bound CtLas1 in two different active states (Pillon et al., 2019). This observation may also provide a structural rationale for the activation of ScLas1 and CtLas1 by Grc3, as well as for the fairly weak activation of CjLas1 by CjGrc3. Of course, since the structure of Las1 analyzed by us lacks the LCT and CC domains, we do not know whether these two domains have an effect on the conformational changes of HEPN domains before and after GRC3 binding.

Discussion

Removal of the ITS2 is the requirement for the maturation of 5.8S rRNA and

25S rRNA, which is an important step during the eukaryotic 60S subunit synthesis. In this study, the structural, biochemical, and functional analysis of ITS2 RNA processing machinery provides a critical step toward understanding the molecular mechanism of Grc3-activated ITS2 processing by Las1 endoribonuclease.

Mechanism of ITS2 processing by Las1-Grc3 dual enzyme complex

Based on our findings, we propose a model of ITS2 processing by Las1 endoribonuclease and its activator Grc3 kinase (Figure 8). In the absence of Grc3, Las1 has very weak ITS2 cleavage activity due to its unstable HEPN dimer. However, in the presence of Grc3, two copies of Las1 and Grc3 assemble into a dynamic tetramer that shows high activity to cleavage ITS2. Las1 initially processes ITS2 at the C2 site, generating a 5.8S rRNA precursor with 2′,3′-cyclic phosphate and a 25S rRNA precursor with 5′-hydroxyl end (Figure 8 and Figure 1I). The second step of ITS2 specific cleavage occurs at the C2′ site to remove the 5′-region of the 25S rRNA precursor. The C2′ cleavage also produces a 5′-hydroxyl product, which is rapidly phosphorylated by Grc3 only in the presence of ATP. After phosphorylation, the 25S precursor is further processed by a Rat1-Rai1 complex with 5′−3′ exonuclease activity, which degrades the 5′-region of the 25S rRNA precursor and subsequently generate mature 25S rRNA (Figure 1I) (Gasse et al., 2015). Furthermore, the nuclear exosome complex drives the maturation of the 5.8S RNA by removing the 3′-end of the precursor through its 3′−5′ exonuclease activity (Fromm et al., 2017).

In addition, based on the structural data, our model may also provide some insight into how Las1-Grc3 complex cleaves ITS2 RNA at both C2 and C2' positions. The Las1-Grc3 tetramer complex has one nuclease active center and two kinase active centers. The nuclease active center consists of two Las1

molecules in a symmetric manner, while the kinase active center consists of only one Grc3 molecule. The ITS2 RNA is predicted to form a stem-loop structure. The symmetrical nuclease active center recognizes the stem region of ITS2 RNA and makes it easy to perform C2 and C2' cleavages on both sides of the stem. C2 and C2' cleavage products are further phosphorylated by two Grc3 kinase active centers, respectively.

Distinct activation mechanism for Las1 HEPN nuclease

Structural and biochemical results highlight the mechanism of Grc3 GCT-mediated Las1 HEPN nuclease activation, which is quite distinct from other HEPN nucleases such as CRISPR-Cas and toxin-antitoxin associated HEPN RNases, Cas13a, Csm6, RnlA. Though proper dimerization of the HEPN domain is critical for HEPN nuclease activity, other factors are also common requirements for HEPN activation. For examples, activation of the Cas13a HEPN enzyme requires target RNA binding and guide-target RNA duplex formation, while allosterically activation of the Csm6 HEPN nuclease is dependent on a cyclic oligoadenylate (Liu, Li, Ma, et al., 2017; Niewoehner et al., 2017). In addition, stimulating the toxicity of RnlA HEPN RNase requires an association between RnlA and RNase HI, and trigging activation of the HEPN domains of Ire1 and RNase L needs binding of ATP to their kinase domains (Lee et al., 2008; Naka, Koga, Yonesaki, & Otsuka, 2014; Wang et al., 2014). It is noteworthy that these activators do not interact directly with the HEPN domain, but bind to other domains to induce a conformational transition of the HEPN domain from inactive to active state. In contrast, Grc3 GCTs bind directly to the active center of HEPN domains and form hydrogen bonds with catalytic residues, which appears to provoke rearrangements of the active site required for activation of HEPN. Regulation of HEPN RNases by interacting with catalytic residues may be a direct and effective measure.

Comparison of Las1-Grc3 complex and other nuclease-kinase machines

Ire1 and RNase L are also nuclease-kinase machines that contain a HEPN domain and a protein kinase domain or a pseudo-protein kinase domain, playing a fundamental role in RNA degradation related to a variety of cellular processes. Although Ire1 and RNase L also require higher-order assembly during RNA degradation, the Las1-Grc3 complex shows distinct structure assembly with them (Figure 8—figure supplement 1). Both the kinase domain and the HEPN domain in Ire1 and RNase L adopt a parallel back to back dimer configuration (Lee et al., 2008; Wang et al., 2014). In Las1, only the HEPN domain forms a dimer architecture, and Grc3 does not contact each other, but binds on both sides to stabilize the HEPN dimer. An ankyrin repeat domain in RNase L and an endoplasmic reticulum (ER) luminal domain in Ire1 has been proposed to promote dimerization of the kinase and HEPN domains (Credle, Finer-Moore, Papa, Stroud, & Walter, 2005; Huang et al., 2014). Whereas the additional CC domain in Las1 is likely to contribute to RNA binding and facilitate cleavage (Figure 4C, D). In addition, Las1, Ire1, and RNase L recognize similar RNA cleavage motifs despite being involved in different RNA processing, splicing, and degradation pathways. Cleavage studies show a preference of Las1 for UAG and UGC motifs, which are also the universal cleavage motifs observed in mRNA decay by Ire1 and RNase L (Pillon & Stanley, 2018).

Materials and methods

Protein expression and purification

For Las1-Grc3 complex expression and purification, *Saccharomyces cerevisiae Las1* (*ScLas1*) *gene* was cloned into pET23a vector with an N-terminal His_6-tag and *Cyberlindnera jadinii* (*CjLas1*) gene was cloned into

pET28a vector with an N-terminal His_6SUMO-tag, while *ScGrc3* and *CjGrc3* genes were cloned into modified pET28a vector containing an N-terminal SUMO-tag, followed by an ubiquitin-like protein1 (Ulp1) protease cleavage site. All recombinant plasmids were transformed into *E.coli* Rosetta (DE3) (Novagen) cells and grown in LB broth at 37°C for 3 h. After culturing to an OD_{600} of 0.6-0.8, protein expression was induced with 0.2 mM isopropyl-1-thio-β-D-galactopyranoside (IPTG) at 16°C for 14 h. For the purification of ScLas1-Grc3 complex proteins, cells expressing ScLas1 proteins and ScGrc3 proteins were collected and co-lysed by sonication in buffer containing 20 mM Tris-HCl, pH 7.5, 500 mM NaCl. After centrifugation, supernatant was incubated with Ni Sepharose (GE Healthcare), and the bound protein was eluted with buffer containing 20 mM Tris-HCl, pH 7.5, 300 mM NaCl, 300 mM imidazole. Eluted protein was digested with Ulp1 protease at 4°C for 2 h and then further purified on a Heparin HP column (GE Healthcare), eluting with a linear gradient of increasing NaCl concentration from 300 mM to 1 M in 20 mM Tris-HCl, pH7.5 buffer. The fractions containing the protein of interest were concentrated and further purified by size-exclusion chromatography (Superdex 200 Increase 10/300, GE Healthcare) in a buffer containing 20 mM Tris-HCl, pH 7.5, 300 mM NaCl, and 1 mM Tris(2-carboxyethyl)phosphine hydrochloride (TCEP). Proteins were collected and concentrated to a final concentration of 15 mg/ml. The mutants and truncations of ScLas1 and ScGrc3 were purified with an identical protocol.

For the purification of CjLas1-Grc3 complex proteins, cells expressing CjLas1 proteins and CjGrc3 proteins were collected and co-lysed by sonication in buffer containing 20 mM Tris-HCl, pH 7.5, 500 mM NaCl. After centrifugation, supernatant was incubated with Ni Sepharose (GE Healthcare), and the bound protein was eluted with buffer containing 20 mM Tris-HCl, pH 7.5, 350 mM NaCl, 300 mM imidazole. Eluted protein was digested with Ulp1 protease at 4°C for 2 h and then further purified on a Heparin HP column (GE Healthcare),

eluting with buffer containing 20 mM Tris-HCl, pH7.5, 1M NaCl. The protein was further purified by size-exclusion chromatography (Superdex 200 Increase 10/300, GE Healthcare) in a buffer containing 20 mM Tris-HCl, pH 7.5, 350 mM NaCl, and 1 mM Tris(2-carboxyethyl)phosphine hydrochloride (TCEP). Proteins were collected and concentrated to a final concentration of 15 mg/ml. Mutants were expressed and purified as wild-type protein. The CjLas1 HEPN construct was purified with an identical protocol.

For the experiment of GST pull-down, the wild-type *ScLas1* gene and its mutants were cloned into a modified pET23a vector (Novagen) with an N-terminal His_6GST-tag, while the wild-type *ScGrc3* gene and its mutants were cloned into a modified pET28a vector containing an N-terminal His_6SUMO-tag. Proteins were overexpressed in *E.coli* Rosetta (DE3) (Novagen) cells and cultured in LB broth to an OD_{600} of 0.6-0.8. Then the target proteins were induced with 0.2 mM isopropyl-1-thio-β-D-galactopyranoside (IPTG) and grown for additional 14 h at 16°C. Cells were collected and lysed by sonication in buffer containing 20 mM Tris-HCl, pH 7.5, 500 mM NaCl. After centrifugation, supernatant was incubated with Ni Sepharose (GE Healthcare), and the bound protein was eluted with buffer containing 20 mM Tris-HCl, pH 7.5, 300 mM NaCl, 300 mM imidazole. The GST-ScLas1 mutants were further purified on a Heparin HP column (GE Healthcare) and ScGrc3 mutants were purified on a HitTrap Q HP column (GE Healthcare). All proteins were further purified by size-exclusion chromatography (Superdex 200 Increase 10/300, GE Healthcare) in a buffer containing 20 mM Tris-HCl, pH 7.5, 300 mM NaCl.

Crystallization, data collection and structure determination

Crystals of ScLas1-Grc3 complex, CjLas1-Grc3 complex and CjLas1 truncated protein (HEPN domain) were first obtained using the sitting drop vapor diffusion method using high-throughput crystallization screening kits (Hampton Research, Molecular Dimensions and QIAGEN). Crystals were then grown in a

mixed solution containing 1 μl complex solution and 1 μl of reservoir solution using the hanging drop vapor diffusion method at 16°C. For growing large crystals, crystals were further optimized by using seeding technique. Well-diffracting crystals of ScLas1-Grc3 complex were grown in a reservoir solution containing 2% (v/v) tacsimate, pH 7.0, 0.1 M imidazole, pH 7.0, 2% (v/v) 2-propanol, and 9% (w/v) PEG 3350. Well-diffracting crystals of CjLas1-Grc3 complex were grown in a reservoir solution containing 0.1 M sodium phosphate, pH 7.5, 0.05 M NaCl, and 9% (w/v) PEG 4000. The best crystals of CjLas1 HEPN domain protein were grown from 0.1 M Tris-HCl, pH 8.0, 0.2 M $MgCl_2$, and 25% (w/v) PEG 3350. All crystals soaked in cryoprotectants made from the mother liquors supplemented with 20% (v/v) glycerol and flash frozen in liquid nitrogen.

All diffraction data sets were collected at beamline BL-17U1, BL-18U1, and BL-19U1 at Shanghai Synchrotron Radiation Facility (SSRF) and National Center for Protein Sciences Shanghai (NCPSS), and processed with HKL3000 (Otwinowski & Minor, 1997). The CjLas1 HEPN structure were determined by molecular replacement using the HEPN domain structure within CtLas1-Grc3 (PDB: 6OF4) as the search model using the program PHENIX Phaser (Adams et al., 2002; Pillon et al., 2019). The phases of ScLas1-Grc3 complex and CjLas1-Grc3 complex were solved by molecular replacement method with the cryo-EM maps of Las1-Grc3 complexes using PHENIX Phaser. The model was manually built and adjusted using the program COOT (Emsley, Lohkamp, Scott, & Cowtan, 2010). Iterative cycles of crystallographic refinement were performed using PHENIX. All data processing and structure refinement statistics are summarized in Supplementary Table 1. Structure figures were prepared using PyMOL (http://www.pymol.org/).

Cryo-EM data acquisition

The samples were diluted at a final concentration of around 1.0 mg/mL. Three

microliters of the samples were applied onto glow-discharged 200-mesh R2/1 Quantifoil copper grids. The grids were blotted for 4 s and rapidly cryocooled in liquid ethane using a Vitrobot Mark IV (Thermo Fisher Scientific) at 4°C and 100% humidity. The samples were imaged in a Titan Krios cryo-electron microscope (Thermo Fisher Scientific) at a magnification of 105,000× (corresponding to a calibrated sampling of 0.82 Å per pixel). Micrographs were recorded by EPU software (Thermo Fisher Scientific) with a K3 detector, where each image was composed of 30 individual frames an exposure time of 3 s and an exposure rate of 16.7 electrons per second per $Å^2$. A total of 2,520 movie stacks for ScLas1-Grc3 complex and 8,616 movie stacks for CjLas1-Grc3 complex were collected.

Single-particle image processing and 3D reconstruction

All micrographs were first imported into Relion (Scheres, 2012) for image processing. The motion-correction was performed using MotionCor2 (Zheng et al., 2017) and the contrast transfer function (CTF) was determined using CTFFIND4 (Rohou & Grigorieff, 2015). All particles were autopicked using the NeuralNet option in EMAN2 (Tang et al., 2007). Then, particle coordinates were imported to Relion, where the poor 2D class averages were removed by several rounds of 2D classification. Initial maps were built and classified using ab-initio 3D reconstruction in cryoSPARC (Punjani, Rubinstein, Fleet, & Brubaker, 2017) without any symmetry applied. Heterogeneous refinement was further performed to remove bad particles using one good and one bad starting maps. The good class having 264,341 particles for ScLas1-Grc3 complex or 523,843 particles for CjLas1-Grc3 complex was selected and subjected to 3D homogeneous refinement, local & global CTF refinement, and non-uniform refinement with C2 symmetry imposed, achieving a 3.07 Å resolution map for the ScLas1-Grc3 complex and a 3.39 Å resolution map for the CjLas1-Grc3 complex, respectively. Resolution for the final maps were estimated with the 0.143 criterion of the Fourier shell correlation curve.

Resolution maps were calculated in cryoSPARC using the “Local Resolution Estimation” option. (More information in Supplementary Figure S2, Supplementary Figure S3, and Supplementary Table 2).

In vitro transcription of RNA

Unlabeled ITS2 RNAs used for cleavage assays were synthesized by *in vitro* transcription with T7 RNA polymerase and linearized plasmid DNAs as templates. Transcription reactions were performed at 37°C for 4 h in buffer containing 100 mM HEPES-KOH, pH 7.9, 20 mM $MgCl_2$, 30 mM DTT, 2 mM each NTP, 2 mM spermidine, 0.1 mg/ml T7 RNA polymerase, and 40 ng/μl linearized plasmid DNA template. The transcribed RNA was then purified by gel electrophoresis on a 12% denaturing (8 M urea) polyacrylamide gel, RNA band was excised from the gel and recovered with Elutrap System. The purified RNA was resuspended in DEPC (diethy pyrocarbonate)-treated water.

In vitro ITS2 RNA cleavage assays

For 5′-Cy5 and 3′-Cy3 labeled ITS2 RNA cleavage assays, 0.5 μM of ITS2 RNA was incubated at 37°C for 2 h with increasing amount of Las1, Grc3 or Las1-Grc3 complex proteins (0.05 μM-0.5 μM) in cleavage buffer containing 20 mM Tris-HCl, pH 7.5, 300 mM NaCl, 1 mM Tris(2-carboxyethyl)phosphine hydrochloride (TCEP). 5′-Cy5 and 3′-Cy3 labeled ITS2 RNA was synthesized from Takara Biomedical Technology. Reactions were stopped by adding 2 × loading buffer. Samples were analyzed on a 20% urea denaturing polyacrylamide gel with TBE buffer. Cleavage products were visualized by fluorescent imaging and analysis system (SINSAGE TECHNOLOGY).

For unlabeled ITS2 RNA cleavage assays, 10 μM of ITS2 RNA was incubated at 37°C for 2 h with increasing amount of Las1, Grc3 or Las1-Grc3 complex proteins (1.5 μM-15 μM) in cleavage buffer containing 20 mM Tris-HCl, pH 7.5, 300 mM NaCl, 1 mM Tris(2-carboxyethyl)phosphine hydrochloride (TCEP). Reactions were stopped by adding 2 × loading buffer

and were then quenched at 75°C for 5 min. Samples were analyzed on a 20% urea denaturing polyacrylamide gel with TBE buffer. Cleavage products were visualized by toluidine blue staining. The experiment was repeated three times.

RNA cleavage products phosphorylation assays

10 μM of unlabeled ITS2 RNA was incubated at 37°C for 1.5 h with 10 μM of Las1-Grc3 complex proteins in cleavage buffer containing 20 mM Tris-HCl, pH 7.5, 300 mM NaCl, 1 mM Tris(2-carboxyethyl)phosphine hydrochloride (TCEP). 1 mM ATP was added into each reaction system at 37°C for 30 min. Reactions were stopped by adding 2 × loading buffer and were then quenched at 75°C for 5 min. Samples were analyzed on a 20% urea denaturing polyacrylamide gel with TBE buffer. Cleavage products were visualized by toluidine blue staining. The experiment was repeated three times.

GST pull-down assays

Pull-down experiments were carried out using GST fusion proteins to analyze the association between Las1 and Grc3. 0.2 mg purified GST-ScLas1 protein were incubated with 0.4 mg purified ScGrc3 protein in binding buffer containing 20 mM Tris-HCl, pH 7.5, 500 mM NaCl, 2 mM DTT. 80 μl GST affinity resin was added into each reaction system at 4°C for 60 min. The resin was washed with 1 ml of binding buffer. After washing five times, the binding samples were eluted with elution buffer containing 20 mM Tris, pH 7.5, 20 mM GSH, 500 mM NaCl, and 2 mM DTT. The elution samples were then monitored using SDS-PAGE (polyacrylamide gel electrophoresis) and visualized by Coomassie blue staining. The assays were quantified by band densitometry. The experiment was repeated three times.

Electrophoretic mobility shift assays

Electrophoretic mobility shift assays (EMSA) were performed with a series of

Las1-Grc3 complex dilutions from 20 μM to 2 μM and a 81-nt ITS2 RNA. the ITS2 RNA was synthesized by in vitro transcription. Proteins were incubated with ITS2 RNA in a binding buffer containing 20 mM Tris-HCl, pH 7.5, 300 mM NaCl for 30 min at 4°C. After reaction, the binding samples were then resolved on 5% native acrylamide gels in Tris-Glycine (0.5X TBE) buffer pH 8.5 under an electric field of 100 volts for 40 min at 4°C. Gels were imaged by using a ChemiDoc XRS+ (Bio-rad). The experiment was repeated three times.

RNA sequencing

Enzyme-digested products from the ITS2 cleavage assay were isolated by dialysis from denaturing polyacrylamide gel. T4 PNK was used to phosphorylate the 5′ terminus of RNA products. After the above treatment, RNA samples were linked with the adaptor RNA by T4 RNA ligase-1. RNA samples were then treated for reverse transcription and PCR amplification. The PCR amplification products were cloned into pET28a vector, then sequenced. The experiment was repeated three times.

Data availability

The atomic coordinates of the reported X-ray and cryo-EM structures have been deposited in the Protein Data Bank (PDB) with the following accession codes: 7Y16 (CjLas1, X-ray), 7Y17 (CjLas1-Grc3 complex, X-ray), 7Y18 (ScLas1-Grc3 complex, X-ray), 8J5Y (ScLas1-Grc3 complex, cryo-EM), and 8J60 (CjLas1-Grc3 complex, cryo-EM). Cryo-EM maps of the ScLas1-Grc3 complex and CjLas1-Grc3 complex in this study have been deposited in the wwPDB OneDep System under EMD accession code EMD-33733 and EMD-33735.

Acknowledgements

We are grateful to the staff of the BL-17U1, BL-18U1 and BL-19U1 beamlines

at the National Center for Protein Sciences Shanghai (NCPSS) at Shanghai Synchrotron Radiation Facility (SSRF). We thank the Cryo-EM Center at the University of Science and Technology of China for the support of cryo-EM data collection.

Author contributions

J.C., H.C., X.L., and R.H. expressed and purified the proteins and grew crystals. J.C., H.C., and L.L. collected X-ray diffraction data. S.L., K.Z., and L.L. solved the structures. X.L., H.C., R.H., and J.C. carried out all of the cloning and performed the biochemical assays. L.L. prepared the figures; L.L. wrote the manuscript and supervised all of the research.

Funding

National Natural Science Foundation of China (32171286).

- Liang Liu

National Natural Science Foundation of China (32022047).

- Liang Liu

The Ministry of Science and Technology of China (2022YFC2303700).

- Kaiming Zhang
- Shanshan Li

The Ministry of Science and Technology of China (2022YFA1302700).

- Kaiming Zhang

The Strategic Priority Research Program of the Chinese Academy of Sciences (XDB0490000).

- Kaiming Zhang

Center for Advanced Interdisciplinary Science and Biomedicine of IHM (QYPY20220019).

- Kaiming Zhang

The Fundamental Research Funds for the Central Universities (WK9100000044).

- Kaiming Zhang

The Fundamental Research Funds for the Central Universities (WK9100000032).

- Shanshan Li

The funders had no role in study design, data collection and interpretation, or the decision to submit the work for publication.

Competing interests

The authors declare no competing interests.

References

Abudayyeh, O. O., Gootenberg, J. S., Konermann, S., Joung, J., Slaymaker, I. M., Cox, D. B., . . . Zhang, F. (2016). C2c2 is a single-component programmable RNA-guided RNA-targeting CRISPR effector. *Science, 353*(6299), aaf5573. doi:10.1126/science.aaf5573

Adams, P. D., Grosse-Kunstleve, R. W., Hung, L. W., Ioerger, T. R., McCoy, A. J., Moriarty, N. W., . . . Terwilliger, T. C. (2002). PHENIX: building new software for automated crystallographic structure determination. *Acta Crystallogr D Biol Crystallogr, 58*(Pt 11), 1948-1954. doi:10.1107/s0907444902016657

Anger, A. M., Armache, J. P., Berninghausen, O., Habeck, M., Subklewe, M., Wilson, D. N., & Beckmann, R. (2013). Structures of the human and Drosophila 80S ribosome. *Nature, 497*(7447), 80-85. doi:10.1038/nature12104

Castle, C. D., Cassimere, E. K., & Denicourt, C. (2012). LAS1L interacts with the mammalian Rix1 complex to regulate ribosome biogenesis. *Mol Biol Cell, 23*(4), 716-728.

667 doi:10.1091/mbc.E11-06-0530

668 Castle, C. D., Cassimere, E. K., Lee, J., & Denicourt, C. (2010). Las1L is a nucleolar protein
669 required for cell proliferation and ribosome biogenesis. *Mol Cell Biol, 30*(18),
670 4404-4414. doi:10.1128/MCB.00358-10

671 Castle, C. D., Sardana, R., Dandekar, V., Borgianini, V., Johnson, A. W., & Denicourt, C.
672 (2013). Las1 interacts with Grc3 polynucleotide kinase and is required for ribosome
673 synthesis in Saccharomyces cerevisiae. *Nucleic Acids Res, 41*(2), 1135-1150.
674 doi:10.1093/nar/gks1086

675 Coleman, A. W. (2003). ITS2 is a double-edged tool for eukaryote evolutionary comparisons.
676 *Trends Genet, 19*(7), 370-375. doi:10.1016/S0168-9525(03)00118-5

677 Cote, C. A., Greer, C. L., & Peculis, B. A. (2002). Dynamic conformational model for the role of
678 ITS2 in pre-rRNA processing in yeast. *RNA, 8*(6), 786-797.
679 doi:10.1017/s1355838202023063

680 Credle, J. J., Finer-Moore, J. S., Papa, F. R., Stroud, R. M., & Walter, P. (2005). On the
681 mechanism of sensing unfolded protein in the endoplasmic reticulum. *Proc Natl Acad*
682 *Sci U S A, 102*(52), 18773-18784. doi:10.1073/pnas.0509487102

683 Doseff, A. I., & Arndt, K. T. (1995). LAS1 is an essential nuclear protein involved in cell
684 morphogenesis and cell surface growth. *Genetics, 141*(3), 857-871.
685 doi:10.1093/genetics/141.3.857

686 Doudna, J. A., & Rath, V. L. (2002). Structure and function of the eukaryotic ribosome: the next
687 frontier. *Cell, 109*(2), 153-156. doi:10.1016/s0092-8674(02)00725-0

688 Emsley, P., Lohkamp, B., Scott, W. G., & Cowtan, K. (2010). Features and development of

689 Coot. *Acta Crystallogr D Biol Crystallogr, 66*(Pt 4), 486-501.
690 doi:10.1107/S0907444910007493
691 Fernandez-Pevida, A., Kressler, D., & de la Cruz, J. (2015). Processing of preribosomal RNA
692 in Saccharomyces cerevisiae. *Wiley Interdiscip Rev RNA, 6*(2), 191-209.
693 doi:10.1002/wrna.1267
694 Fromm, L., Falk, S., Flemming, D., Schuller, J. M., Thoms, M., Conti, E., & Hurt, E. (2017).
695 Reconstitution of the complete pathway of ITS2 processing at the pre-ribosome. *Nat*
696 *Commun, 8*(1), 1787. doi:10.1038/s41467-017-01786-9
697 Gasse, L., Flemming, D., & Hurt, E. (2015). Coordinated Ribosomal ITS2 RNA Processing by
698 the Las1 Complex Integrating Endonuclease, Polynucleotide Kinase, and
699 Exonuclease Activities. *Mol Cell, 60*(5), 808-815. doi:10.1016/j.molcel.2015.10.021
700 Gordon, J., Pillon, M. C., & Stanley, R. E. (2019). Nol9 Is a Spatial Regulator for the Human
701 ITS2 Pre-rRNA Endonuclease-Kinase Complex. *J Mol Biol, 431*(19), 3771-3786.
702 doi:10.1016/j.jmb.2019.07.007
703 Granneman, S., Petfalski, E., & Tollervey, D. (2011). A cluster of ribosome synthesis factors
704 regulate pre-rRNA folding and 5.8S rRNA maturation by the Rat1 exonuclease. *EMBO*
705 *J, 30*(19), 4006-4019. doi:10.1038/emboj.2011.256
706 Holm, L., & Rosenstrom, P. (2010). Dali server: conservation mapping in 3D. *Nucleic Acids*
707 *Res, 38*(Web Server issue), W545-549. doi:10.1093/nar/gkq366
708 Huang, H., Zeqiraj, E., Dong, B., Jha, B. K., Duffy, N. M., Orlicky, S., . . . Sicheri, F. (2014).
709 Dimeric structure of pseudokinase RNase L bound to 2-5A reveals a basis for
710 interferon-induced antiviral activity. *Mol Cell, 53*(2), 221-234.

doi:10.1016/j.molcel.2013.12.025

Khatter, H., Myasnikov, A. G., Natchiar, S. K., & Klaholz, B. P. (2015). Structure of the human 80S ribosome. *Nature, 520*(7549), 640-645. doi:10.1038/nature14427

Knott, G. J., East-Seletsky, A., Cofsky, J. C., Holton, J. M., Charles, E., O'Connell, M. R., & Doudna, J. A. (2017). Guide-bound structures of an RNA-targeting A-cleaving CRISPR-Cas13a enzyme. *Nat Struct Mol Biol, 24*(10), 825-833. doi:10.1038/nsmb.3466

Korennykh, A. V., Egea, P. F., Korostelev, A. A., Finer-Moore, J., Zhang, C., Shokat, K. M., . . . Walter, P. (2009). The unfolded protein response signals through high-order assembly of Ire1. *Nature, 457*(7230), 687-693. doi:10.1038/nature07661

Lafontaine, D. L. (2015). Noncoding RNAs in eukaryotic ribosome biogenesis and function. *Nat Struct Mol Biol, 22*(1), 11-19. doi:10.1038/nsmb.2939

Lee, K. P., Dey, M., Neculai, D., Cao, C., Dever, T. E., & Sicheri, F. (2008). Structure of the dual enzyme Ire1 reveals the basis for catalysis and regulation in nonconventional RNA splicing. *Cell, 132*(1), 89-100. doi:10.1016/j.cell.2007.10.057

Liu, L., Li, X., Ma, J., Li, Z., You, L., Wang, J., . . . Wang, Y. (2017). The Molecular Architecture for RNA-Guided RNA Cleavage by Cas13a. *Cell, 170*(4), 714-726 e710. doi:10.1016/j.cell.2017.06.050

Liu, L., Li, X., Wang, J., Wang, M., Chen, P., Yin, M., . . . Wang, Y. (2017). Two Distant Catalytic Sites Are Responsible for C2c2 RNase Activities. *Cell, 168*(1-2), 121-134 e112. doi:10.1016/j.cell.2016.12.031

Naka, K., Koga, M., Yonesaki, T., & Otsuka, Y. (2014). RNase HI stimulates the activity of

RnlA toxin in Escherichia coli. *Mol Microbiol, 91*(3), 596-605. doi:10.1111/mmi.12479

Niewoehner, O., Garcia-Doval, C., Rostol, J. T., Berk, C., Schwede, F., Bigler, L., . . . Jinek, M. (2017). Type III CRISPR-Cas systems produce cyclic oligoadenylate second messengers. *Nature, 548*(7669), 543-548. doi:10.1038/nature23467

Otwinowski, Z., & Minor, W. (1997). Processing of X-ray diffraction data collected in oscillation mode. *Methods Enzymol, 276*, 307-326.

Pillon, M. C., Goslen, K. H., Gordon, J., Wells, M. L., Williams, J. G., & Stanley, R. E. (2020). It takes two (Las1 HEPN endoribonuclease domains) to cut RNA correctly. *J Biol Chem, 295*(18), 5857-5870. doi:10.1074/jbc.RA119.011193

Pillon, M. C., Hsu, A. L., Krahn, J. M., Williams, J. G., Goslen, K. H., Sobhany, M., . . . Stanley, R. E. (2019). Cryo-EM reveals active site coordination within a multienzyme pre-rRNA processing complex. *Nat Struct Mol Biol, 26*(9), 830-839. doi:10.1038/s41594-019-0289-8

Pillon, M. C., Sobhany, M., Borgnia, M. J., Williams, J. G., & Stanley, R. E. (2017). Grc3 programs the essential endoribonuclease Las1 for specific RNA cleavage. *Proc Natl Acad Sci U S A, 114*(28), E5530-E5538. doi:10.1073/pnas.1703133114

Pillon, M. C., & Stanley, R. E. (2018). Nuclease integrated kinase super assemblies (NiKs) and their role in RNA processing. *Curr Genet, 64*(1), 183-190. doi:10.1007/s00294-017-0749-9

Punjani, A., Rubinstein, J. L., Fleet, D. J., & Brubaker, M. A. J. N. m. (2017). cryoSPARC: algorithms for rapid unsupervised cryo-EM structure determination. *14*(3), 290-296.

Rohou, A., & Grigorieff, N. J. J. o. s. b. (2015). CTFFIND4: Fast and accurate defocus

755 estimation from electron micrographs. *192*(2), 216-221.

756 Scheres, S. H. J. J. o. s. b. (2012). RELION: implementation of a Bayesian approach to

757 cryo-EM structure determination. *180*(3), 519-530.

758 Schillewaert, S., Wacheul, L., Lhomme, F., & Lafontaine, D. L. (2012). The evolutionarily

759 conserved protein Las1 is required for pre-rRNA processing at both ends of ITS2. *Mol*

760 *Cell Biol, 32*(2), 430-444. doi:10.1128/MCB.06019-11

761 Tang, G., Peng, L., Baldwin, P. R., Mann, D. S., Jiang, W., Rees, I., & Ludtke, S. J. J. J. o. s. b.

762 (2007). EMAN2: an extensible image processing suite for electron microscopy. *157*(1),

763 38-46.

764 Tomecki, R., Sikorski, P. J., & Zakrzewska-Placzek, M. (2017). Comparison of preribosomal

765 RNA processing pathways in yeast, plant and human cells - focus on coordinated

766 action of endo- and exoribonucleases. *FEBS Lett, 591*(13), 1801-1850.

767 doi:10.1002/1873-3468.12682

768 Wang, Y., Li, Y., Toth, J. I., Petroski, M. D., Zhang, Z., & Zhao, J. C. (2014).

769 N6-methyladenosine modification destabilizes developmental regulators in embryonic

770 stem cells. *Nat Cell Biol, 16*(2), 191-198. doi:10.1038/ncb2902

771 Wilson, D. N., & Doudna Cate, J. H. (2012). The structure and function of the eukaryotic

772 ribosome. *Cold Spring Harb Perspect Biol, 4*(5). doi:10.1101/cshperspect.a011536

773 Woolford, J. L., Jr., & Baserga, S. J. (2013). Ribosome biogenesis in the yeast

774 Saccharomyces cerevisiae. *Genetics, 195*(3), 643-681.

775 doi:10.1534/genetics.113.153197

776 Wu, S., Tutuncuoglu, B., Yan, K., Brown, H., Zhang, Y., Tan, D., . . . Gao, N. (2016). Diverse

roles of assembly factors revealed by structures of late nuclear pre-60S ribosomes. *Nature, 534*(7605), 133-137. doi:10.1038/nature17942

Xiang, S., Cooper-Morgan, A., Jiao, X., Kiledjian, M., Manley, J. L., & Tong, L. (2009). Structure and function of the 5'-->3' exoribonuclease Rat1 and its activating partner Rai1. *Nature, 458*(7239), 784-788. doi:10.1038/nature07731

Zhang, C., Konermann, S., Brideau, N. J., Lotfy, P., Wu, X., Novick, S. J., . . . Lyumkis, D. (2018). Structural Basis for the RNA-Guided Ribonuclease Activity of CRISPR-Cas13d. *Cell, 175*(1), 212-223 e217. doi:10.1016/j.cell.2018.09.001

Zheng, S. Q., Palovcak, E., Armache, J.-P., Verba, K. A., Cheng, Y., & Agard, D. A. J. N. m. (2017). MotionCor2: anisotropic correction of beam-induced motion for improved cryo-electron microscopy. *14*(4), 331-332.

Figure Legends

Figure 1. ScLas1 specifically cleaves ITS2 at C2 and C2′ sites. (A) 33-nt ITS2 RNA with 5′-Cy5 and 3′-Cy3 labels. **(B)** *In vitro* RNA cleavage assay using 5′-Cy5 and 3′-Cy3 labeled 33-nt RNA. **(C)** *In vitro* RNA cleavage assay of unlabeled 33-nt RNA. **(D)** 81-nt ITS2 RNA. **(E)** *In vitro* RNA cleavage assay of unlabeled 81-nt RNA. **(F)** RNA-sequencing traces from ScLas1-cleaved ITS2 products P2 and P4. **(G)** RNA phosphorylation assay with ScLas1-Grc3 complex. **(H)** RNA degradation assay with ScRat1-Rai1 complex. **(I)** The ITS2 pre-rRNA processing pathway. All cleavage experiments were repeated three times.

The following figure supplements are available for Figure 1:

Figure 1 – Figure Supplement 1. CjGrc3-activated CjLas1-catalytic ITS2 pre-rRNA cleavage.

Figure 1 – Figure Supplement 2. ScGrc3 has no ITS2 pre-rRNA cleavage activity.

Figure 1 – Figure Supplement 3. Catalytic residues of Las1 HEPN domain are necessary for ITS2 pre-rRNA cleavage.

Figure 1 – Figure Supplement 4. Characterization of the metal independence of ITS2 pre-rRNA cleavage.

Figure 2. Overall structure of ScLas1-Grc3 complex. (A) Domain organization of ScLas1 and ScGrc3. **(B)** Ribbon representations of ScLas1-Grc3 complex. Color-coding used for Las1 and Grc3 is identical to that used in Fig. 2a. **(C)** Surface representations of ScLas1-Grc3 complex. Color-coding used for Las1 and Grc3 is identical to that used in Figure 2A.

The following figure supplement is available for Figure 2:

Figure 2 – Figure Supplement 1. Single-particle cryo-EM analysis of the ScLas1-Grc3 complex. (A) Representative motion-corrected cryo-EM micrograph. **(B)** Reference-free 2D class averages. **(C)** Workflow of the data processing. **(D)** Euler angle distribution of the particle images. **(E)** Gold standard FSC plot for the 3D reconstruction with full particle set, calculated in cryoSPARC. **(F)** Resolution map for the final 3D reconstruction.

Figure 3. Overall structure of CjLas1-Grc3 complex. (A) Domain organization of CjLas1 and CjGrc3. **(B)** (Top) Ribbon representations of CjLas1-Grc3 complex. Color-coding used for Las1 and Grc3 is identical to that used in Fig. 3a. (Bottom) A diagram showing how the Las1-Grc3 tetramer is formed. **(C)** (Top) Surface representations of CjLas1-Grc3 complex. Color-coding used for Las1 and Grc3 is identical to that used in Figure 3A.

(Bottom) A diagram showing how the Las1-Grc3 tetramer is formed.

The following figure supplements are available for Figure 3:

Figure 3 – Figure Supplement 1. Single-particle cryo-EM analysis of the CjLas1-Grc3 complex. (A) Representative motion-corrected cryo-EM micrograph. **(B)** Reference-free 2D class averages. **(C)** Workflow of the data processing. **(D)** Euler angle distribution of the particle images. **(E)** Gold standard FSC plot for the 3D reconstruction with full particle set, calculated in cryoSPARC. **(F)** Resolution map for the final 3D reconstruction.

Figure 3 – Figure Supplement 2. Comparison of cryo-EM and crystal structures of Las1-Grc3 complexes. (A) Superposition of the ScLas1-Grc3 complex crystal structure with the cryo-EM structure. Color-coding used for ScLas1 and ScGrc3 in crystal structure is identical to that used in Fig. 2a. ScLas1 and ScGrc3 in cryo-EM structure are colored in gray. **(B)** Superposition of the CjLas1-Grc3 complex crystal structure with the cryo-EM structure. Color-coding used for CjLas1 and CjGrc3 in crystal structure is identical to that used in Fig. 3a. CjLas1 and CjGrc3 in cryo-EM structure are colored in gray.

Figure 3 – Figure Supplement 3. Sequence alignment of Las1 proteins. The ScLas1 protein was aligned with its respective homologs. Alignment was performed using the MUSCLE program. The secondary structures of ScLas1 and CjLas1 are shown above and below the sequences, respectively. Conserved residues are highlighted in yellow, and invariant residues are highlighted in red. Catalytic residues in Las1 HEPN domain are marked in violet triangles. The figure was prepared using ESPript3.

Figure 4. The CC domain contributes to ITS2 RNA binding and cleavage. (A) Structural comparison between ScLas1-Grc3 complex and CjLas1-Grc3 complex. Color-coding used for ScLas1 and ScGrc3 is identical to that used in

Fig. 2a. The CC domain of CjLas1 is colored in salmon, other domains of CjLas1 and all domains of CjGrc3 are colored in gray. **(B)** Structures of CjLas1 CC domain (in salmon) and ScLas1 CC domain (in lightmagenta). **(C)** *In vitro* RNA cleavage assay using indicated truncations of ScLas1. HEPN: residues 1-165, CC: residues 181-430, LCT: residues 430-502. **(D)** Electrophoretic mobility shift assay using indicated truncations of ScLas1. All experiments were repeated three times.

Figure 5. ScGrc3 GCT mediates the ITS2 cleavage activity of ScLas1. (A) The crystal structure shows that ScGrc3 GCT binds at an active channel of ScLas1 HEPN dimer. Two HEPN domains of Las1 are colored in pink and violet, respectively. GCTs of Grc3 are colored in teal. The catalytic site is highlighted in yellow. HEPN domains are shown as surfaces, while GCTs are shown as sticks. **(B)** Detailed interactions between ScGrc3 GCT and ScLas1 HEPN domain. **(C)** Sequence alignments of Grc3 GCTs. Identical residues are highlighted in red. Basically constant residuals are shaded in blue. Conserved residues are shaded in orange. **(D)** *In vitro* enzymatic assay of mutations of ScGrc3 residues Glu614, His615 and Trp617. **(E)** GST pull-down experiment assaying the ability of ScGrc3 mutants to interact with ScLas1. **(F)** *In vitro* enzymatic assay of alanine mutations of ScGrc3 C-terminal residues. All experiments were repeated three times.

The following figure supplements are available for Figure 5:

Figure 5 – Figure Supplement 1. The cryo-EM data shows the interactions between ScGrc3 GCTs and ScLas1 HEPN domains.

Figure 5 – Figure Supplement 2. Comparison of crystal structure and cryo-EM structure of HEPN domains and GCTs in ScLas1-Grc3 complex

Figure 5 – Figure Supplement 3. The cryo-EM data (Top) and the crystal data (Bottom) show the electron density of the catalytic site of ScLas1 and the

GCTs of ScGrc3.

Figure 5 – Figure Supplement 4. *In vitro* enzymatic assay of alanine mutations of conserved CjGrc3 residues Trp618, Arg601, Arg606 and Arg607.

Figure 6. Las1 LCT drives Las1-Grc3 cross talk. (A) The crystal structure shows that ScLas1 LCT binds to the CTD domain of ScGrc3. ScGrc3 is shown as surface, ScLas1 LCT is shown as stick. **(B)** Detailed interactions between C-terminal residues of ScLas1 LCT and ScGrc3 CTD domain. **(C)** Detailed interactions between N-terminal residues of ScLas1 LCT and ScGrc3 CTD domain.

The following figure supplements are available for Figure 6:

Figure 6 – Figure Supplement 1. The cryo-EM data shows the interactions between ScLas1 LCT and ScGrc3 CTD domain.

Figure 6 – Figure Supplement 2. Denaturing gel showing the ITS2 pre-RNA cleavage by mutation or deletion of the interacting residues of ScLas1 LCT. All cleavage experiments were repeated three times.

Figure 6 – Figure Supplement 3. GST pull-down experiment assaying the Grc3 binding ability by mutation or deletion of the interacting residues of ScLas1 LCT. All experiments were repeated three times.

Figure 7. Activation mechanism of Las1 by Grc3. (A) Crystal structure of CjLas1 HEPN domain. **(B)** The HEPN3 molecule (in slate) and its symmetry-related molecule (in bluewhite) in Las1 HEPN domain structure. **(C)** The HEPN1 (in pink) and HEPN2 (in violet) molecules in Las1 HEPN domain structure. **(D)** Structural comparison of HEPN dimers between CjLas1-Grc3 complex (Las1A HEPN in pink, Las1B HEPN in violet) and CjLas1 HEPN domain (in gray). Inset: a magnified view of the comparison of the catalytic site in the two structures.

The following figure supplements are available for Figure 7:

Figure 7 – Figure Supplement 1. Structural superposition of HEPN3 (in slate) and its symmetry-related molecule (in bluewhite) with the HEPN1(in pink)-HEPN2 (in violet) dimer.

Figure 7 – Figure Supplement 2. Structural comparison of HEPN dimers between ScLas1-Grc3 complex (Las1A HEPN in pink, Las1B HEPN in violet) and CjLas1 HEPN domain (in gray). Inset: a magnified view of the comparison of the catalytic site in the two structures.

Figure 7 – Figure Supplement 3. (A) Structural comparison of catalytic sites between ScLas1-Grc3 complex (Las1A HEPN in pink, Las1B HEPN in violet) and CtLas1-Grc3 complex in state 1 (in gray, PDB code: 6of3). **(B)** Structural comparison of catalytic sites between CjLas1-Grc3 complex (Las1A HEPN in pink, Las1B HEPN in violet) and CtLas1-Grc3 complex in state 2 (in gray, PDN code: 6of2).

Figure 8. Model for Grc3-mediated Las1-catalyzed ITS2 pre-rRNA processing. Prior to assembly with Grc3, Las1 shows weak processing activity for ITS2 precursor RNA. When combined with Grc3 to form a tetramer complex, Las1 shows high processing activity for ITS2 precursor RNA. Las1 specifically cleaves ITS2 at C2 and C2′ sites to generate 5′-OH terminus products. The 5′-OH terminus products are further phosphorylated by Grc3 when in the presence of ATP.

The following figure supplement is available for Figure 8:

Figure 8 – Figure Supplement 1. Comparison of Las1-Grc3, Ire1 and RNase L. Comparison of structural assembly, activation and substrate recognition mechanisms of Las1-Grc3, Ire1 and RNase L. Two HEPN domains in Las1, Ire1 and RNase L are colored in pink and violet, respectively. Two PNK domains in Grc3, two Kinase domains in Ire1, and two Preudo-Kinase

domains in RNase L, are colored in cyan and greencyan, respectively. The catalytic site is highlighted with a yellow box.

Table 1. Crystallographic data collection and refinement statistics.

	ScLas1-Grc3	CjLas1-Grc3	CjLas1
Data collection*			
Space group	*C*2	$C222_1$	$P2_12_12_1$
Cell dimensions			
a, *b*, *c* (Å)	233.6, 116.1, 159.3	152.6, 240.0, 237.0	51.5, 59.0, 158.7
α, β, γ (°)	90.0, 96.4, 90.0	90.0, 90.0, 90.0	90.0, 90.0, 90.0
Resolution (Å)	50.00-3.50 (3.56-3.50)	50.00-3.23 (3.29-3.23)	50.00-1.80 (1.83-1.80)
R_{merge}	0.298 (0.980)	0.344 (0.958)	0.103 (0.929)
$I/\sigma I$	4.8 (1.1)	4.3 (1.6)	22.0 (2.5)
Completeness (%)	98.8 (96.5)	99.9 (99.9)	97.7 (95.8)
Redundancy	4.5 (3.5)	7.5 (6.4)	10.1 (9.5)
Refinement			
Resolution (Å)	3.69	3.39	1.80
No. reflections	36,773	41,321	44,296
R_{work} / R_{free}	0.2798/0.3151	0.3041/0.3281	0.2120/0.2334
No. atoms			
protein	22,873	18,763	3,657
Water	180	386	212
B-factors (Å^2)			
Protein	95.5	125.6	23.3
Water	33.2	55.9	28.5
R.m.s. deviations			
Bond length (Å)	0.008	0.011	0.015
Bond angles (°)	1.516	1.785	1.500
Ramachandran plot			
Favored region	94.96	95.72	97.98
Allowed region	4.86	4.28	2.02
Outlier region	0.18	0.00	0.00

* Highest resolution shell is shown in parentheses.

Table 2. Cryo-EM data collection, refinement and validation statistics.

	ScLas1-Grc3	CjLas1-Grc3
Data collection and processing		
Microscope	Titan Krios	Titan Krios
Voltage (kV)	300	300
Camera	Gatan K3	Gatan K3
Magnification	105,000x	105,000x
Pixel size (Å)	0.82	0.82
Total exposure (e-/Å^2)	50	50
Exposure time (s)	3	3
Number of frames per exposure	30	30
Energy filter slit width (keV)	20	20
Data collection software	EPU	EPU
Defocus range (μm)	-1.3 - -2.7	-1.2 - -3
Number of micrographs	2,520	8,616
Number of initial particles	525,213	2,215,555
Symmetry	C2	C2
Number of final particles	264,341	523,843
Resolution (0.143 gold standard FSC, Å)	3.07	3.39
Local resolution range (Å)	2.8-4.8	2.8-4.8
Microscope	Titan Krios	Titan Krios
Refinement		
Model composition		
Nonhydrogen atoms	11,212	10,013
Protein residues	1,426	1,339
B-factors (Å^2)		
Protein	92.58	85.58
R.m.s. deviations		
Bond length (Å)	0.009	0.004
Bond angles (°)	1.055	0.849
Validation		
MolProbity score	2.90	2.69
Clashscore	20.56	18.60
Rotamer outliers (%)	8.75	7.86
Ramachandran plot		
Favored region	94.46	96.38
Allowed region	4.83	3.31
Outlier region	0.71	0.31

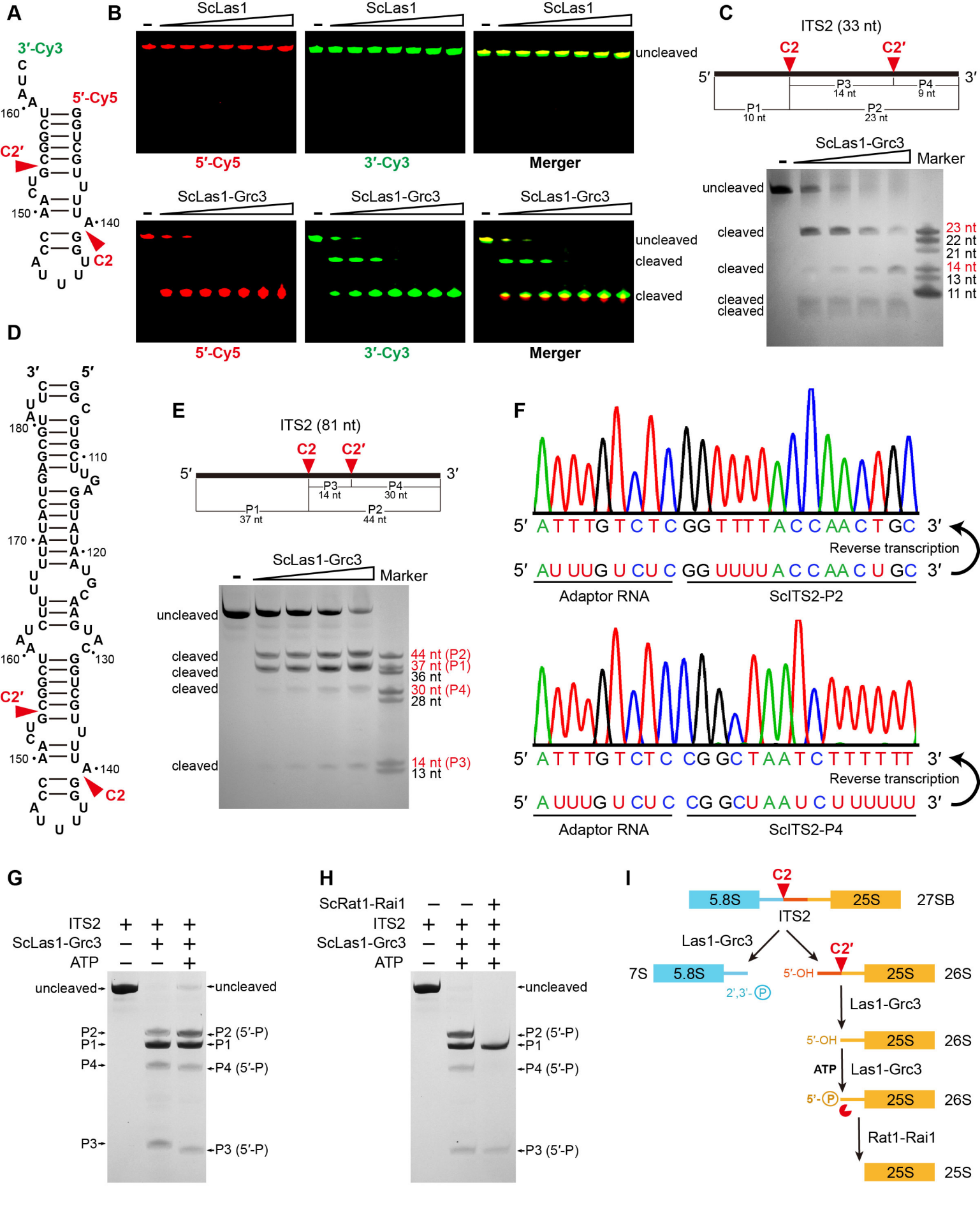
A
3′-Cy3
5′-Cy5
C2′
C2
B
ScLas1
ScLas1-Grc3
uncleaved
cleaved
5′-Cy5
3′-Cy3
Merger
C
ITS2 (33 nt)
C2
C2′
5′
3′
P1
10 nt
P2
23 nt
P3
14 nt
P4
9 nt
ScLas1-Grc3
Marker
uncleaved
cleaved
23 nt
22 nt
21 nt
14 nt
13 nt
11 nt
D
E
ITS2 (81 nt)
P1
37 nt
P2
44 nt
P3
14 nt
P4
30 nt
44 nt (P2)
37 nt (P1)
36 nt
30 nt (P4)
28 nt
14 nt (P3)
13 nt
F
Reverse transcription
Adaptor RNA
ScITS2-P2
ScITS2-P4
G
ITS2
ScLas1-Grc3
ATP
uncleaved
P2
P1
P4
P3
P2 (5′-P)
P4 (5′-P)
P3 (5′-P)
H
ScRat1-Rai1
I
5.8S
25S
27SB
ITS2
Las1-Grc3
7S
26S
5′-OH
2′,3′-P
ATP
Rat1-Rai1

Figure 1

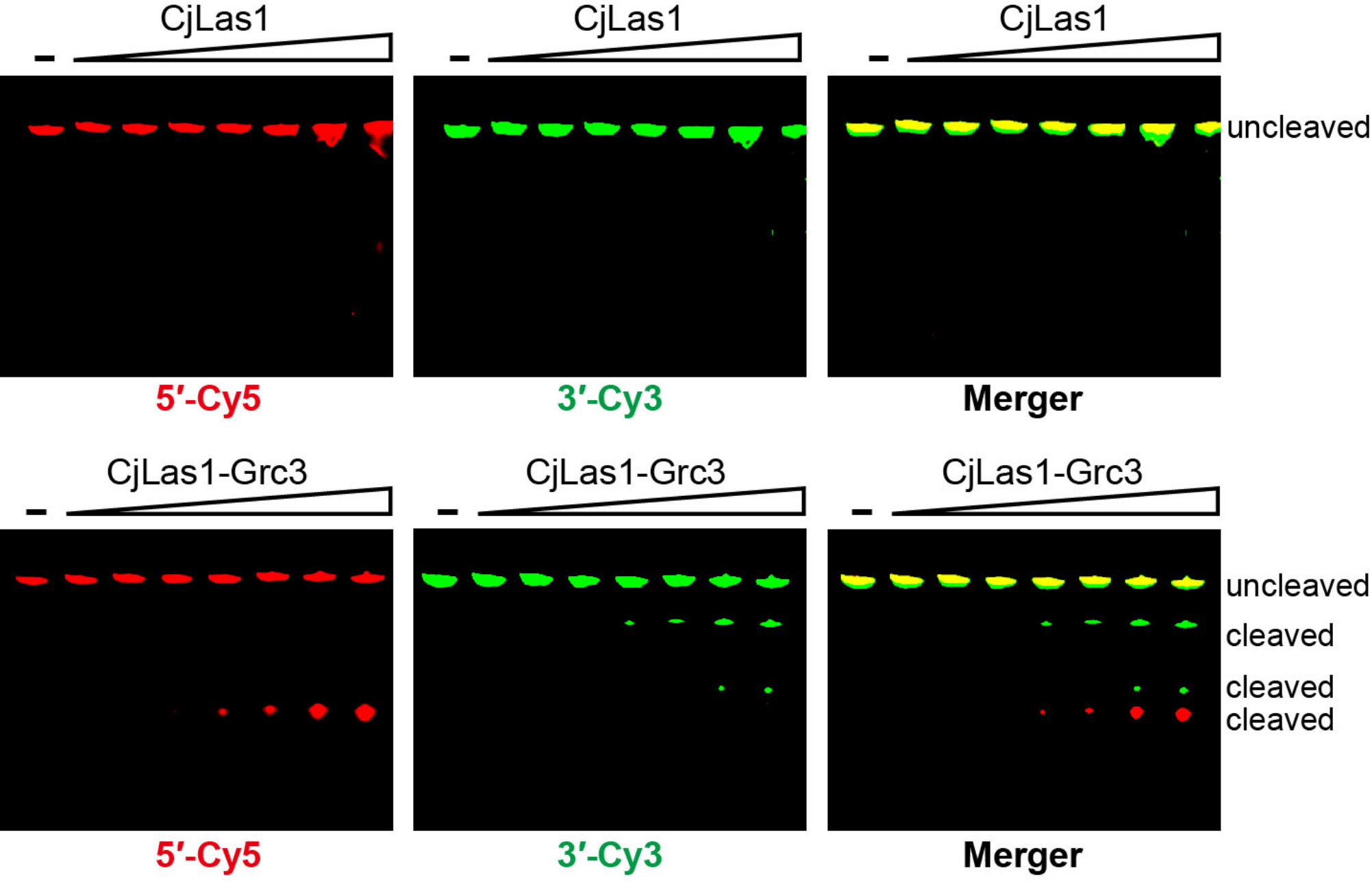

Figure 1—figure supplement 1

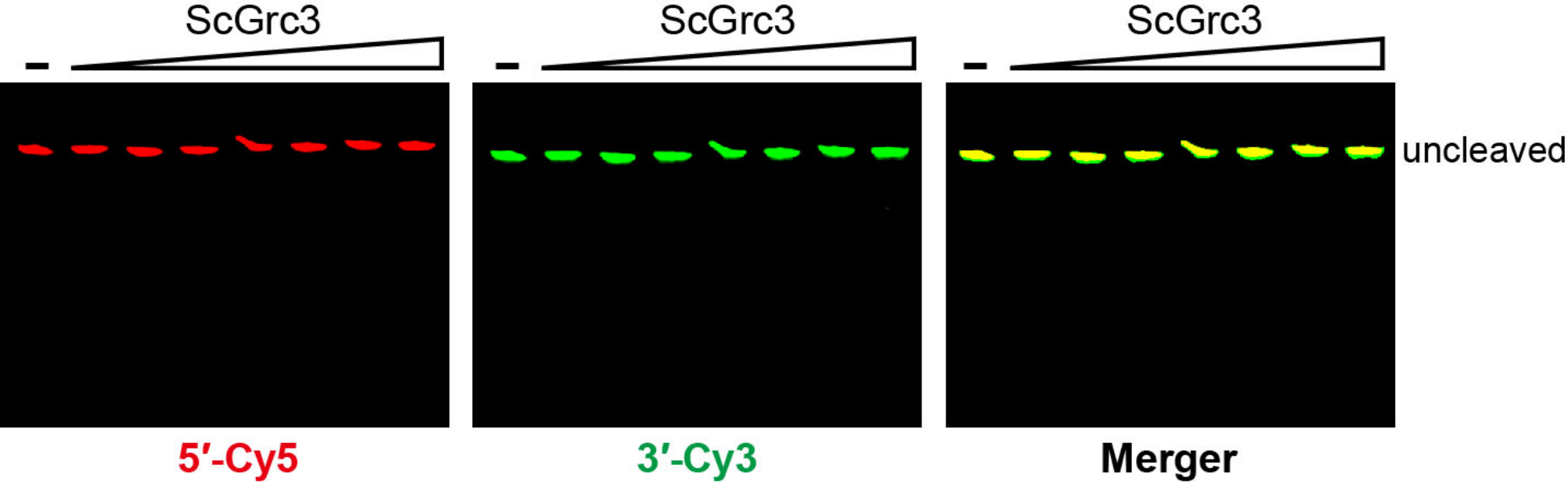

Figure 1—figure supplement 2

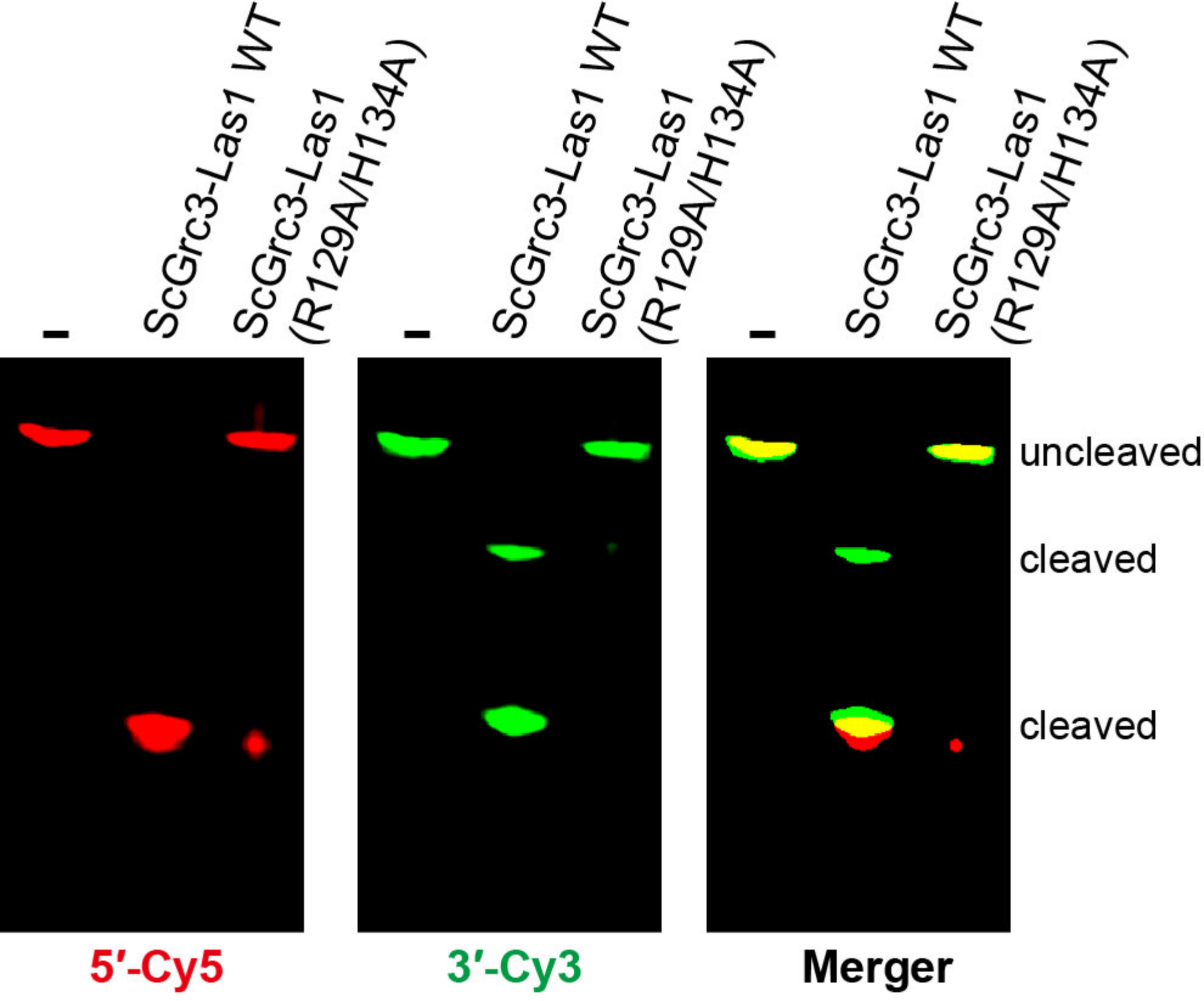

Figure 1—figure supplement 3

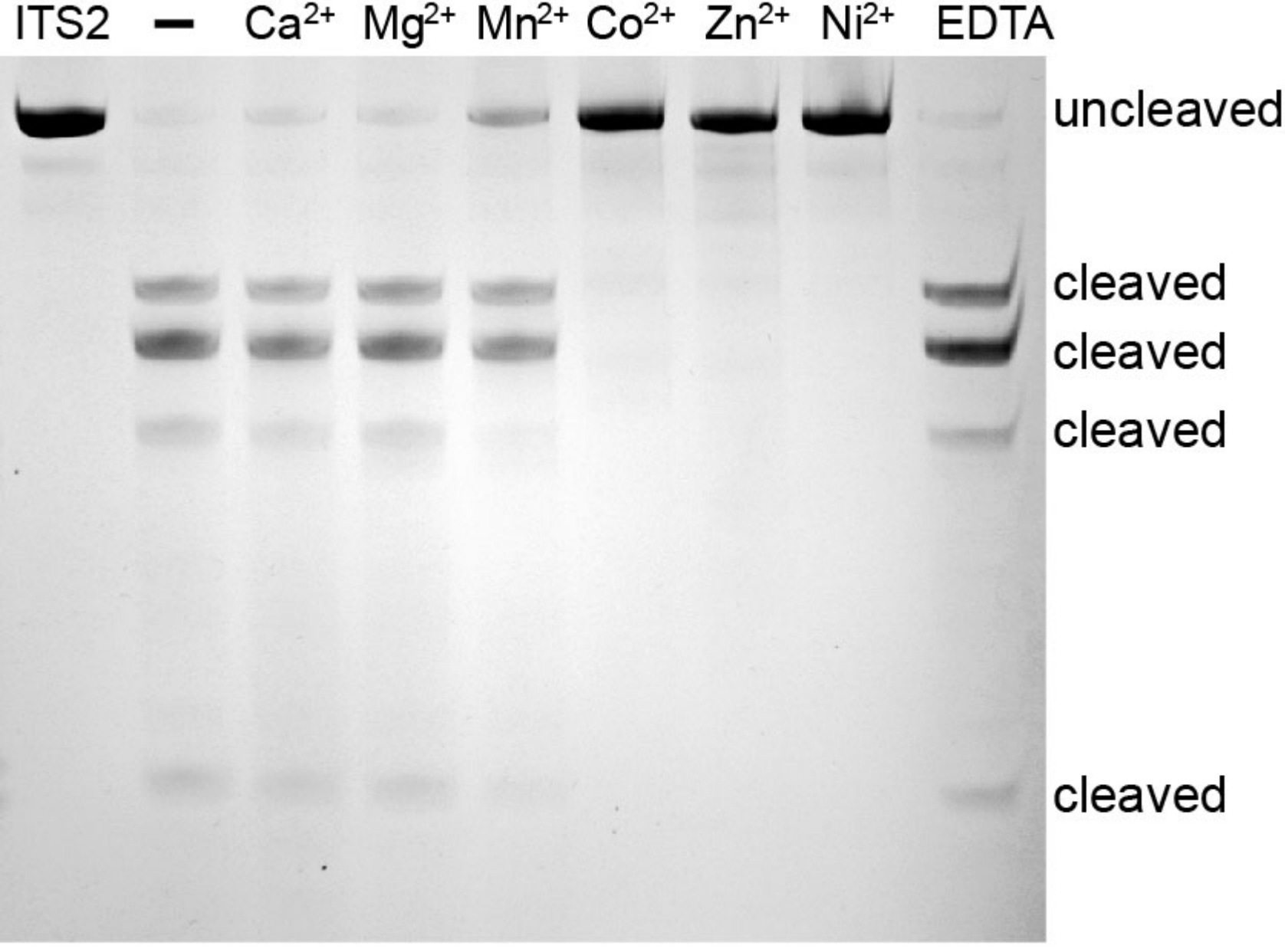

Figure 1—figure supplement 4

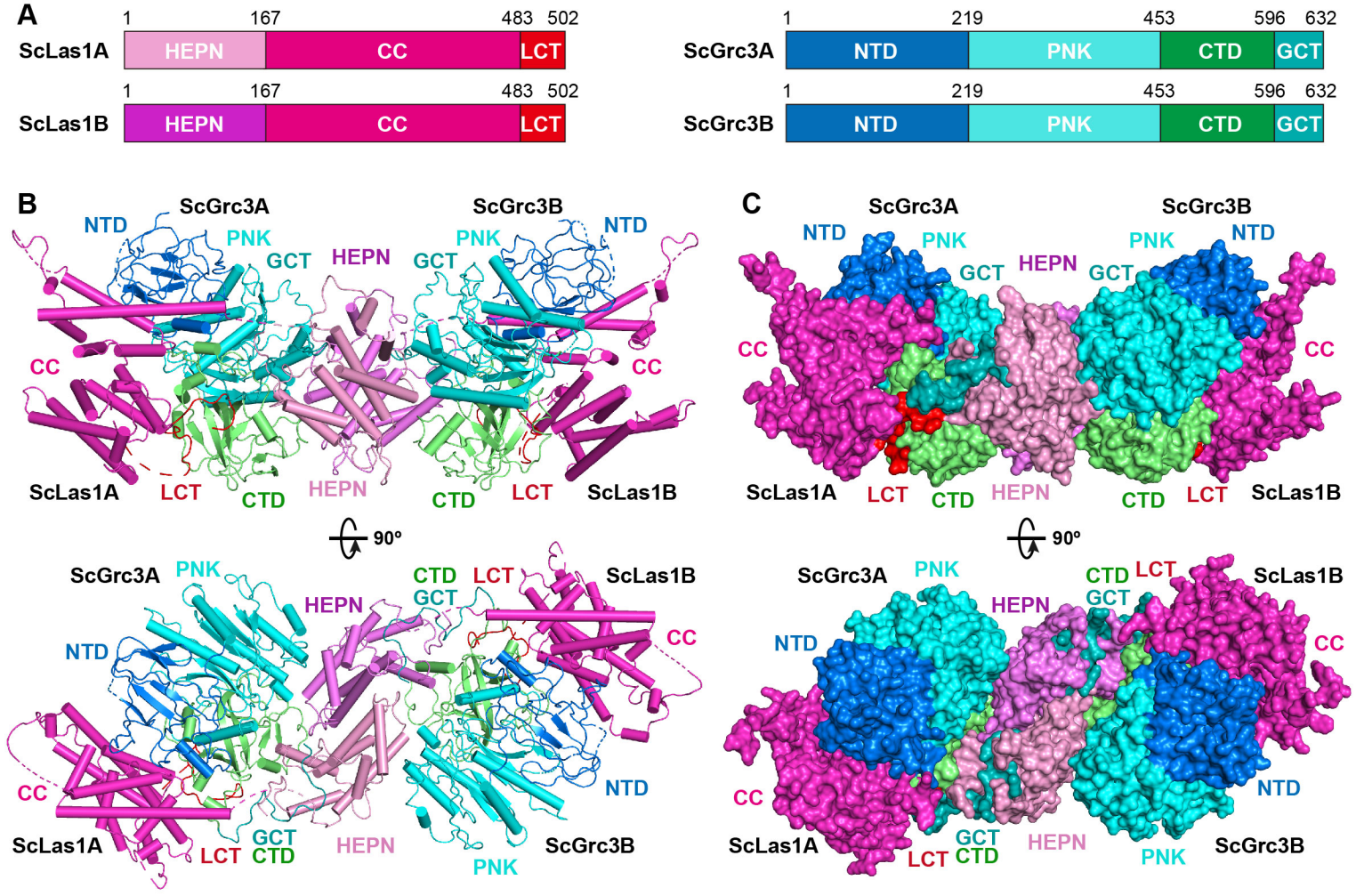
A
ScLas1A
1
167
483
502
HEPN
CC
LCT
ScLas1B
1
167
483
502
HEPN
CC
LCT
ScGrc3A
1
219
453
596
632
NTD
PNK
CTD
GCT
ScGrc3B
1
219
453
596
632
NTD
PNK
CTD
GCT
B
ScGrc3A
ScGrc3B
NTD
PNK
GCT
HEPN
CC
ScLas1A
LCT
CTD
ScLas1B
90°
C
ScGrc3A
ScGrc3B
NTD
PNK
GCT
HEPN
CC
ScLas1A
LCT
CTD
ScLas1B
90°

Figure 2

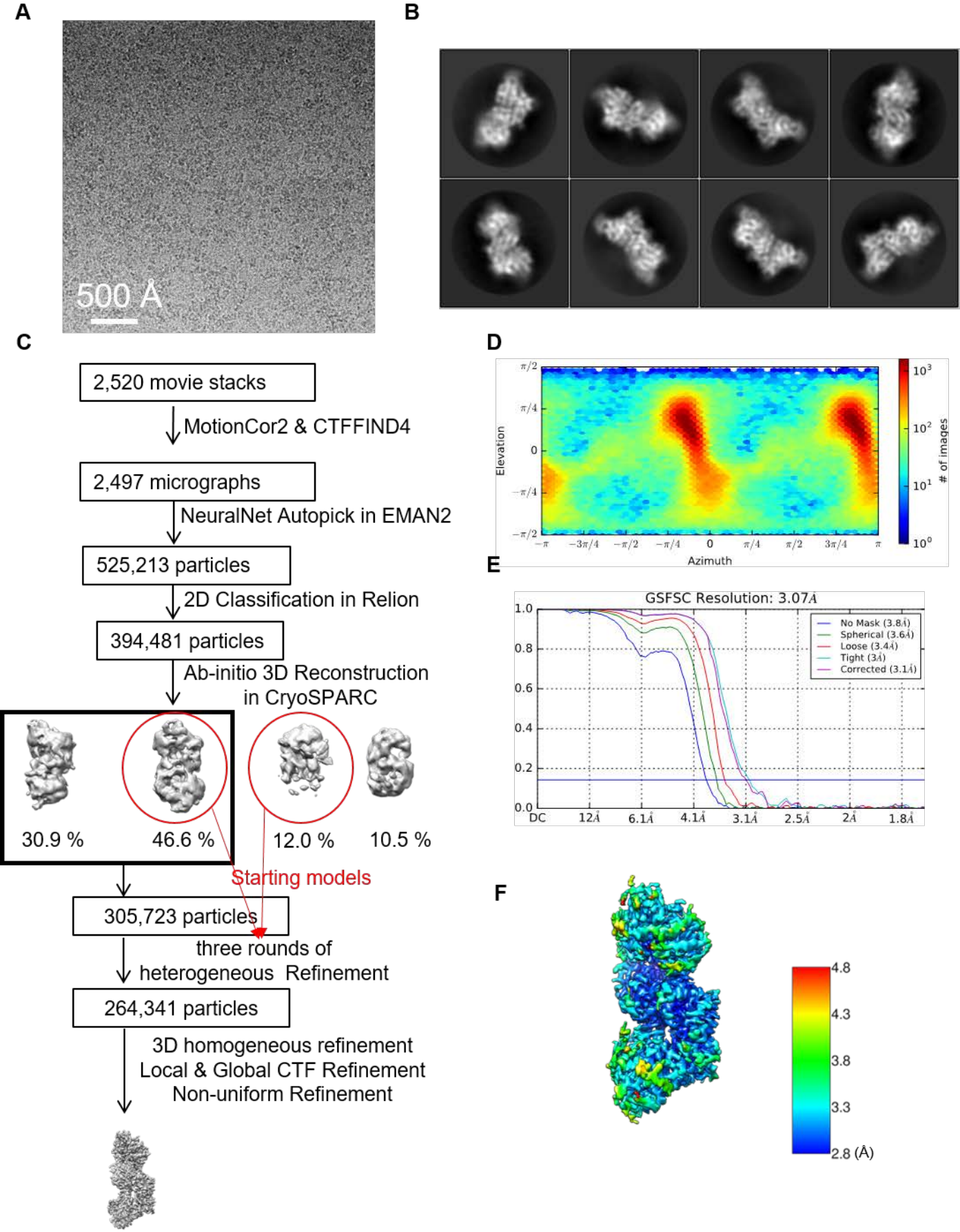

Figure 2-figure supplement 1

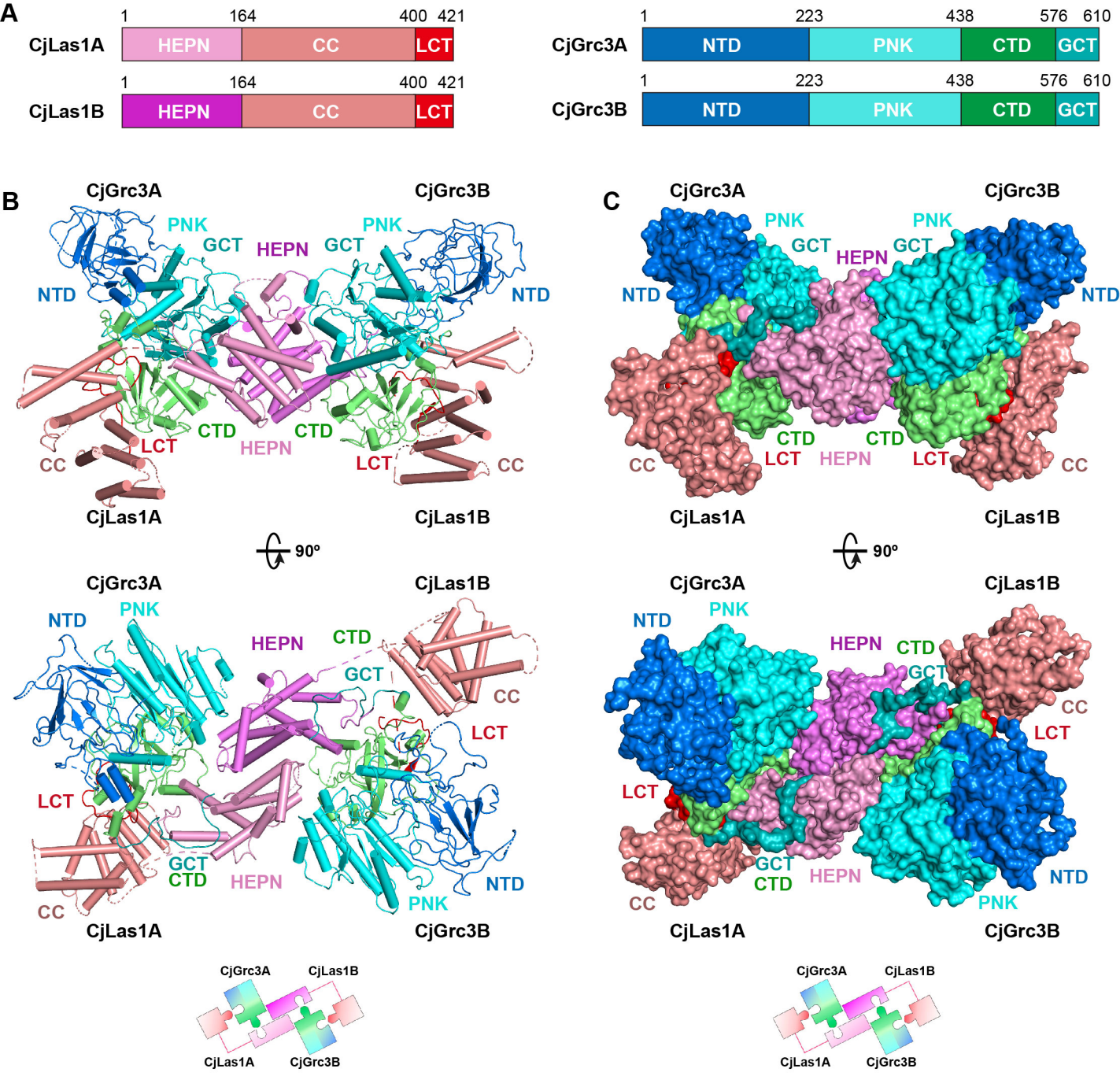
A
CjLas1A
1
164
400
421
HEPN
CC
LCT
CjLas1B
CjGrc3A
223
438
576
610
NTD
PNK
CTD
GCT
CjGrc3B
B
C
90°

Figure 3

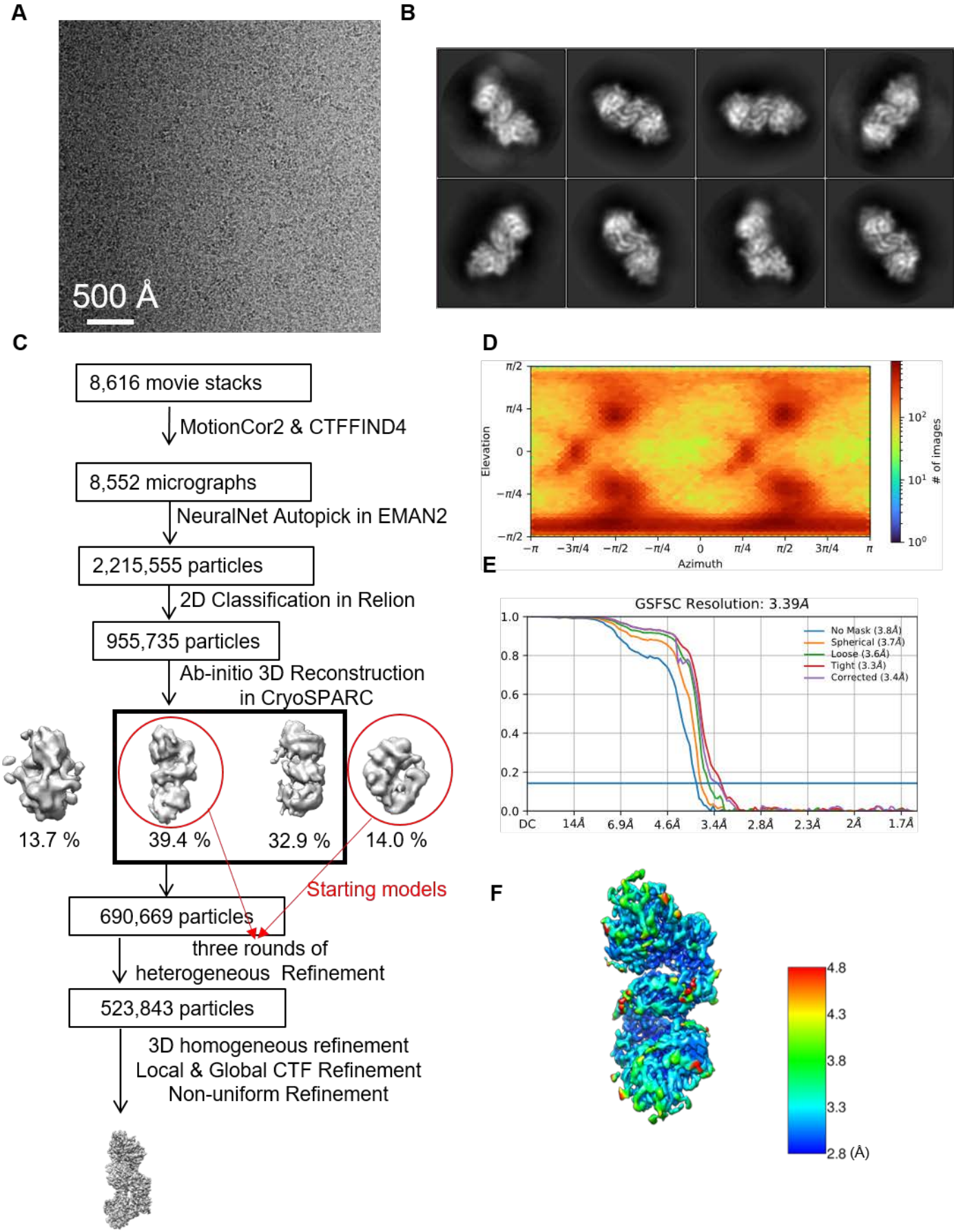

Figure 3—figure supplement 1

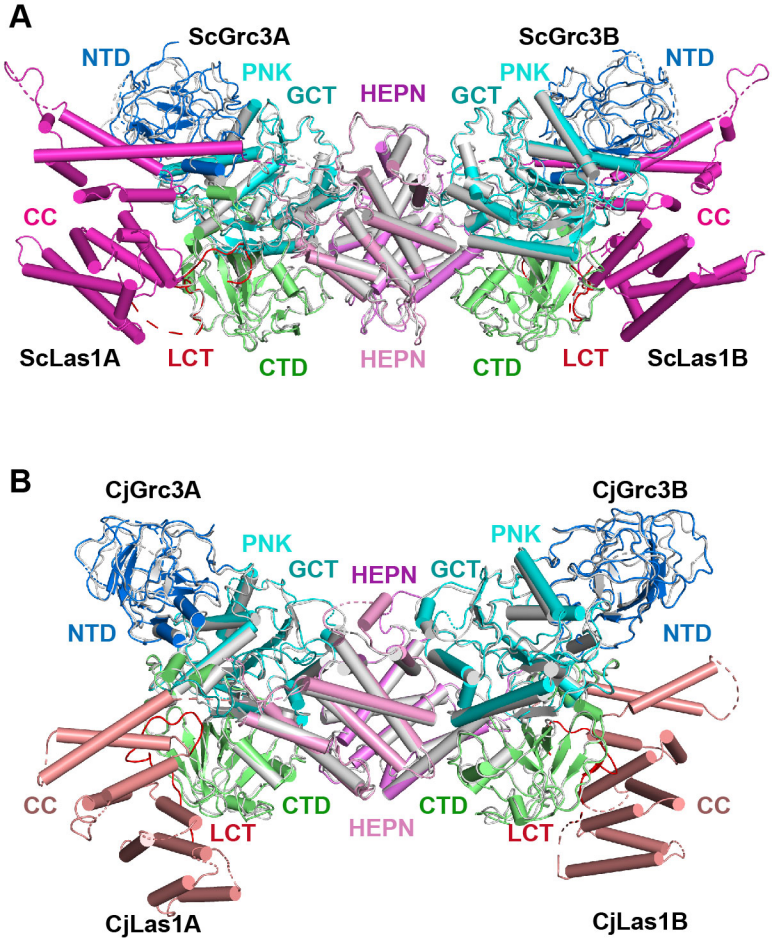

Figure 3—figure supplement 2

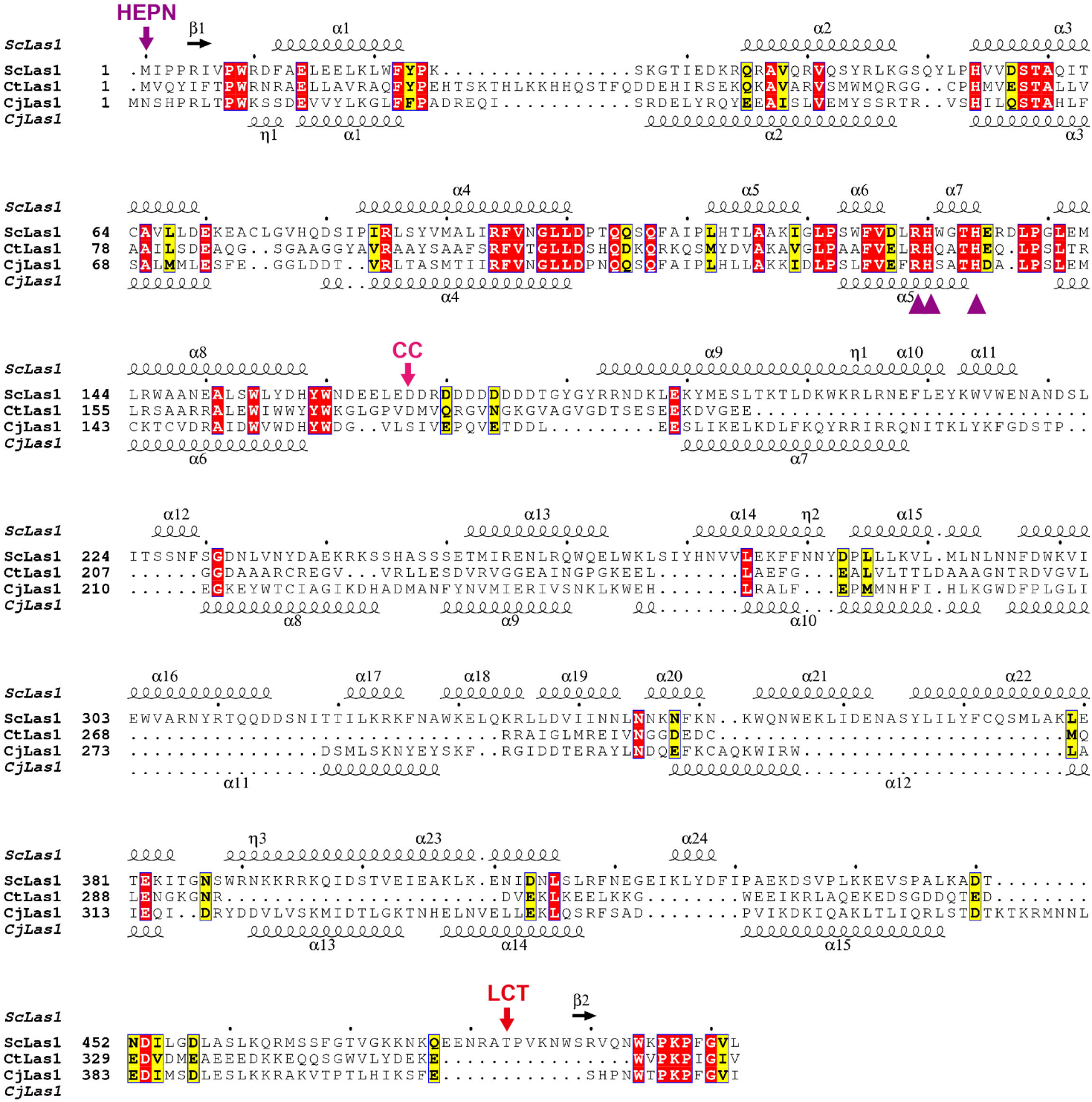

Figure 3—figure supplement 3

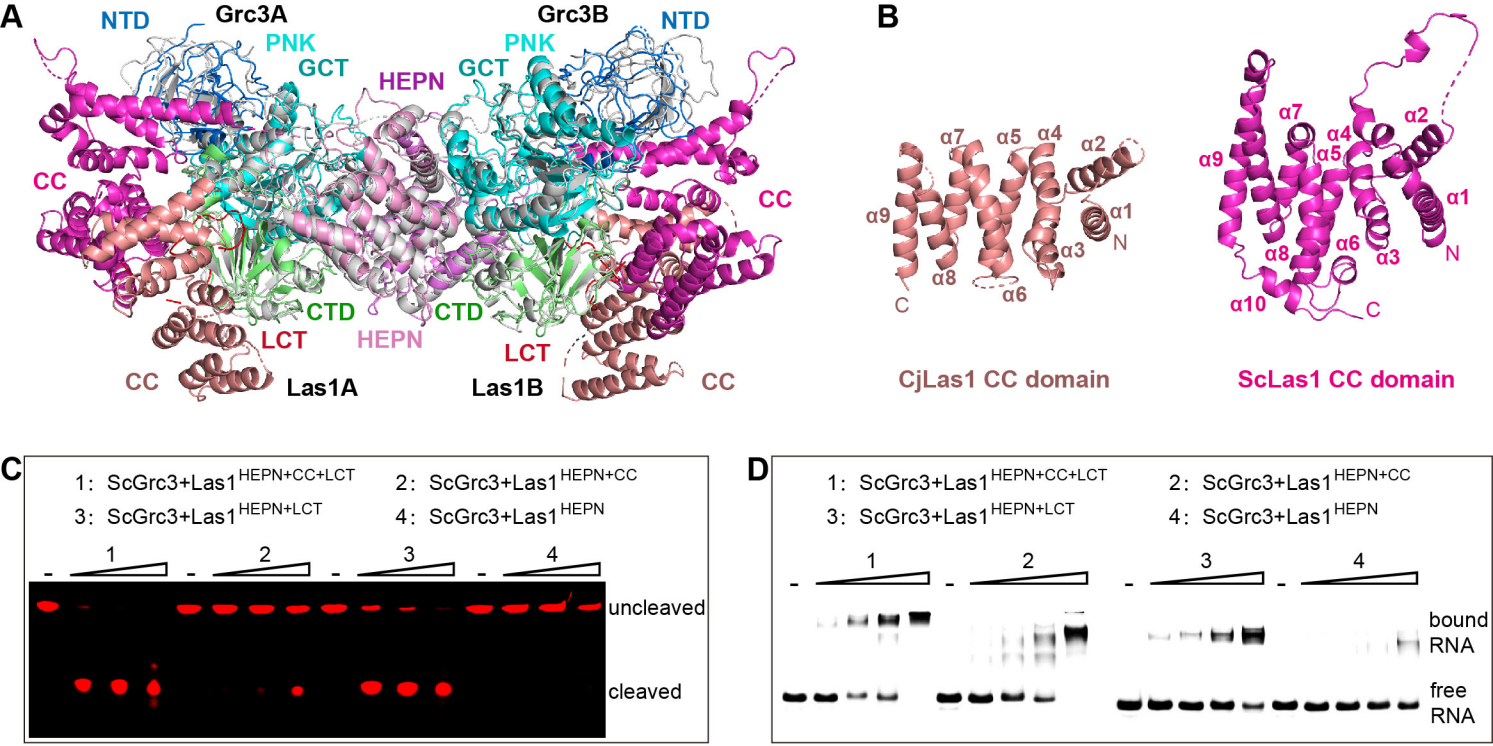
A
NTD
Grc3A
PNK
GCT
HEPN
Grc3B
PNK
GCT
NTD
CC
CC
CTD
CTD
LCT
HEPN
LCT
CC
Las1A
Las1B
CC
B
α7
α5
α4
α2
α9
α1
N
α3
α8
α6
C
CjLas1 CC domain
α7
α2
α4
α5
α9
α1
α8
α6
α3
N
α10
C
ScLas1 CC domain
C
1: ScGrc3+Las1HEPN+CC+LCT
2: ScGrc3+Las1HEPN+CC
3: ScGrc3+Las1HEPN+LCT
4: ScGrc3+Las1HEPN
1
2
3
4
uncleaved
cleaved
D
1: ScGrc3+Las1HEPN+CC+LCT
2: ScGrc3+Las1HEPN+CC
3: ScGrc3+Las1HEPN+LCT
4: ScGrc3+Las1HEPN
1
2
3
4
bound RNA
free RNA

Figure 4

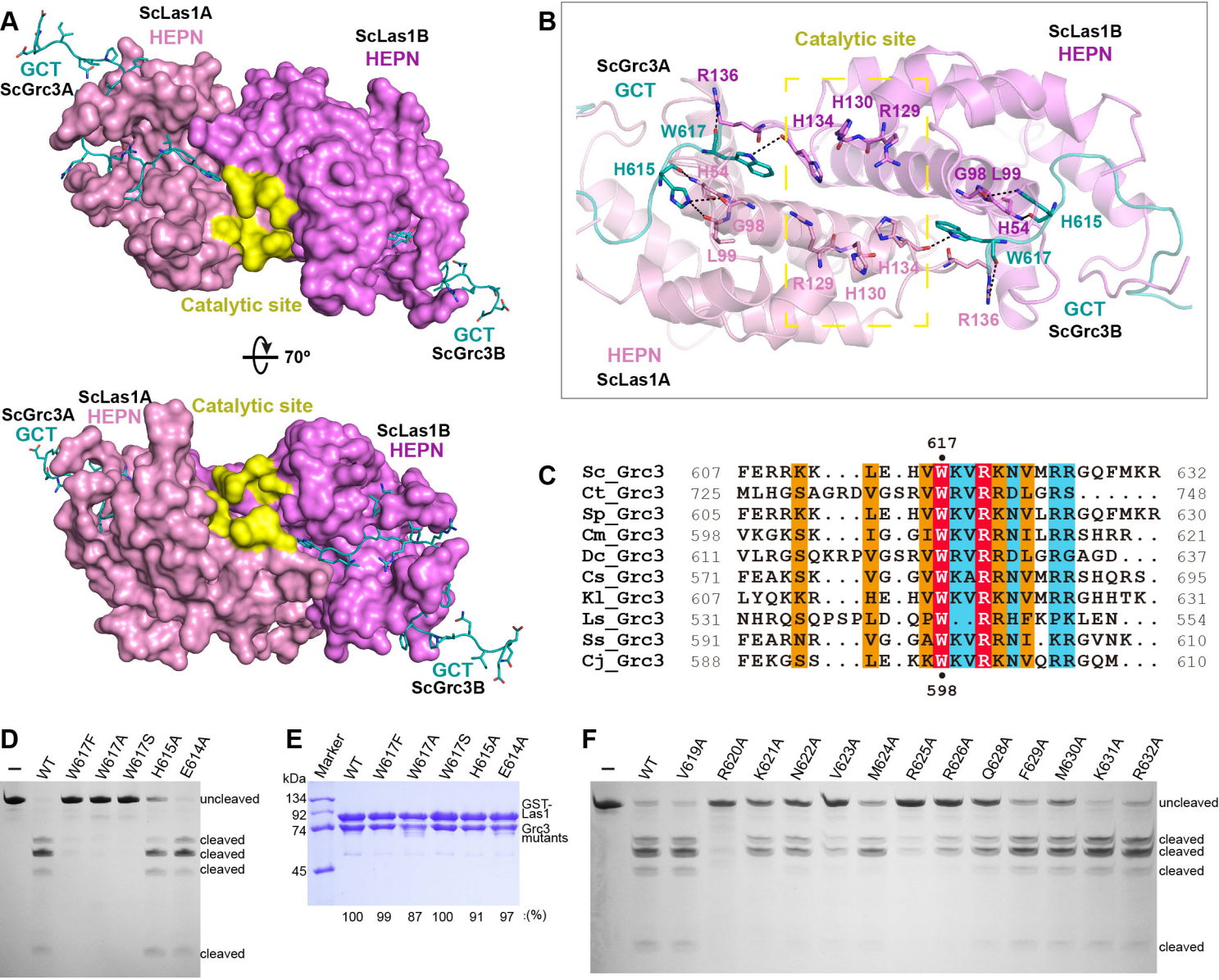
A
ScLas1A
HEPN
GCT
ScGrc3A
ScLas1B
HEPN
Catalytic site
GCT
ScGrc3B
70°
ScLas1A
HEPN
ScGrc3A
GCT
Catalytic site
ScLas1B
HEPN
GCT
ScGrc3B
B
Catalytic site
ScLas1B
HEPN
ScGrc3A
GCT
R136
H130
R129
H134
W617
H615
H54
G98
L99
G98 L99
H615
H54
W617
L99
H134
R129
H130
R136
GCT
ScGrc3B
HEPN
ScLas1A
C
617
Sc_Grc3 607 FERRKK...LE.HVWKVRKNVMRRGQFMKR 632
Ct_Grc3 725 MLHGSAGRDVGSRVWRVRRDLGRS..... 748
Sp_Grc3 605 FERRKK...LE.HVWKVRKNVLRRGQFMKR 630
Cm_Grc3 598 VKGKSK...IG.GIWKVRRNILRRSHRR.. 621
Dc_Grc3 611 VLRGSQKRPVGSRVWRVRRDLGRGAGD... 637
Cs_Grc3 571 FEAKSK...VG.GVWKARRNVMRRSHQRS. 695
Kl_Grc3 607 LYQKKR...HE.HVWKVRKNVMRRGHHTK. 631
Ls_Grc3 531 NHRQSQPSPLD.QPW..RRHFKPKLEN... 554
Ss_Grc3 591 FEARNR...VG.GAWKVRRNI.KRGVNK.. 610
Cj_Grc3 588 FEKGSS...LE.KKWKVRKNVQRRGQM... 610
598
D
–
WT
W617F
W617A
W617S
H615A
E614A
uncleaved
cleaved
cleaved
cleaved
cleaved
E
Marker
WT
W617F
W617A
W617S
H615A
E614A
kDa
134
92
74
45
GST-Las1
Grc3 mutants
100 99 87 100 91 97 :(%)
F
–
WT
V619A
R620A
K621A
N622A
V623A
M624A
R625A
R626A
Q628A
F629A
M630A
K631A
R632A
uncleaved
cleaved
cleaved
cleaved
cleaved

Figure 5

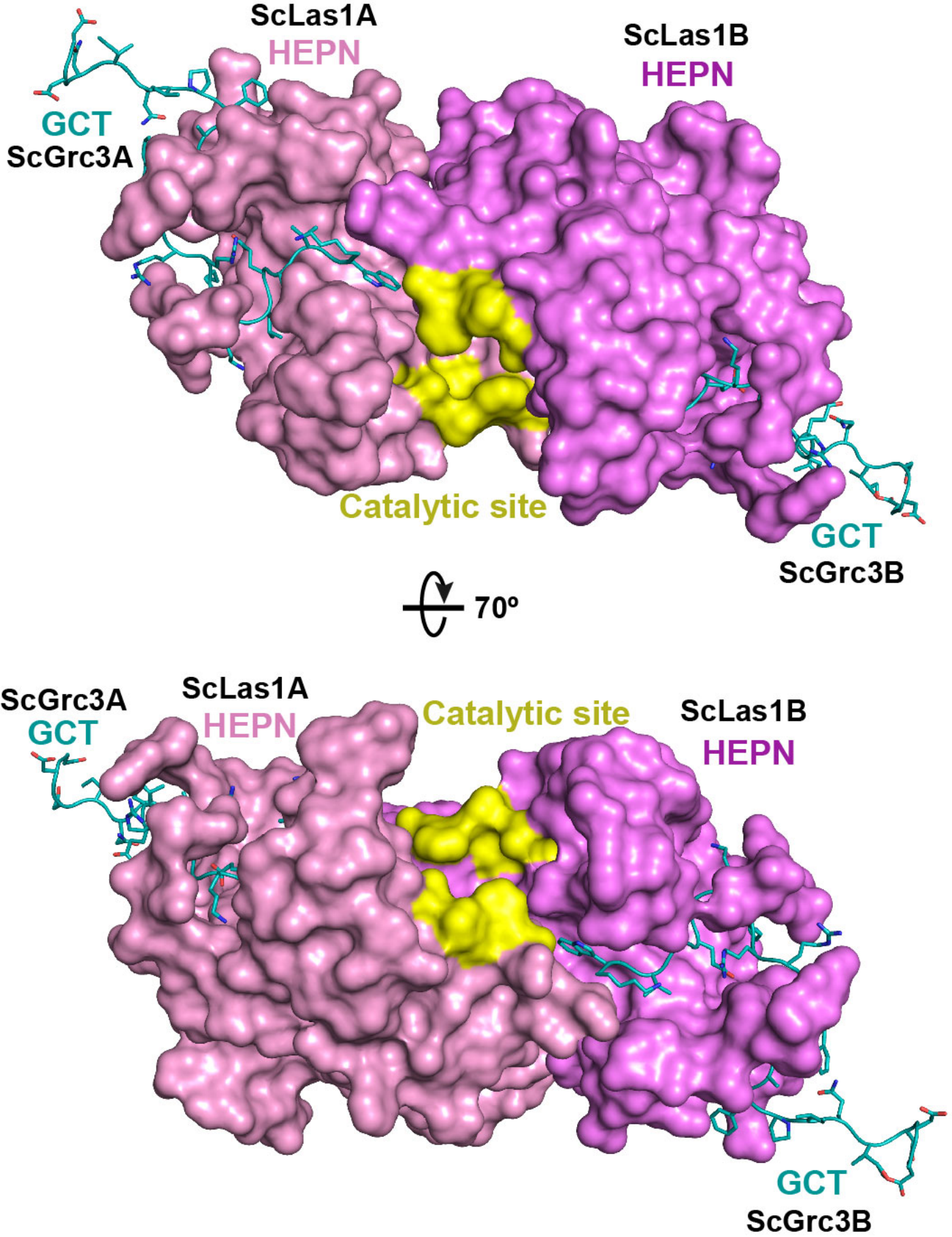

Figure 5—figure supplement 1

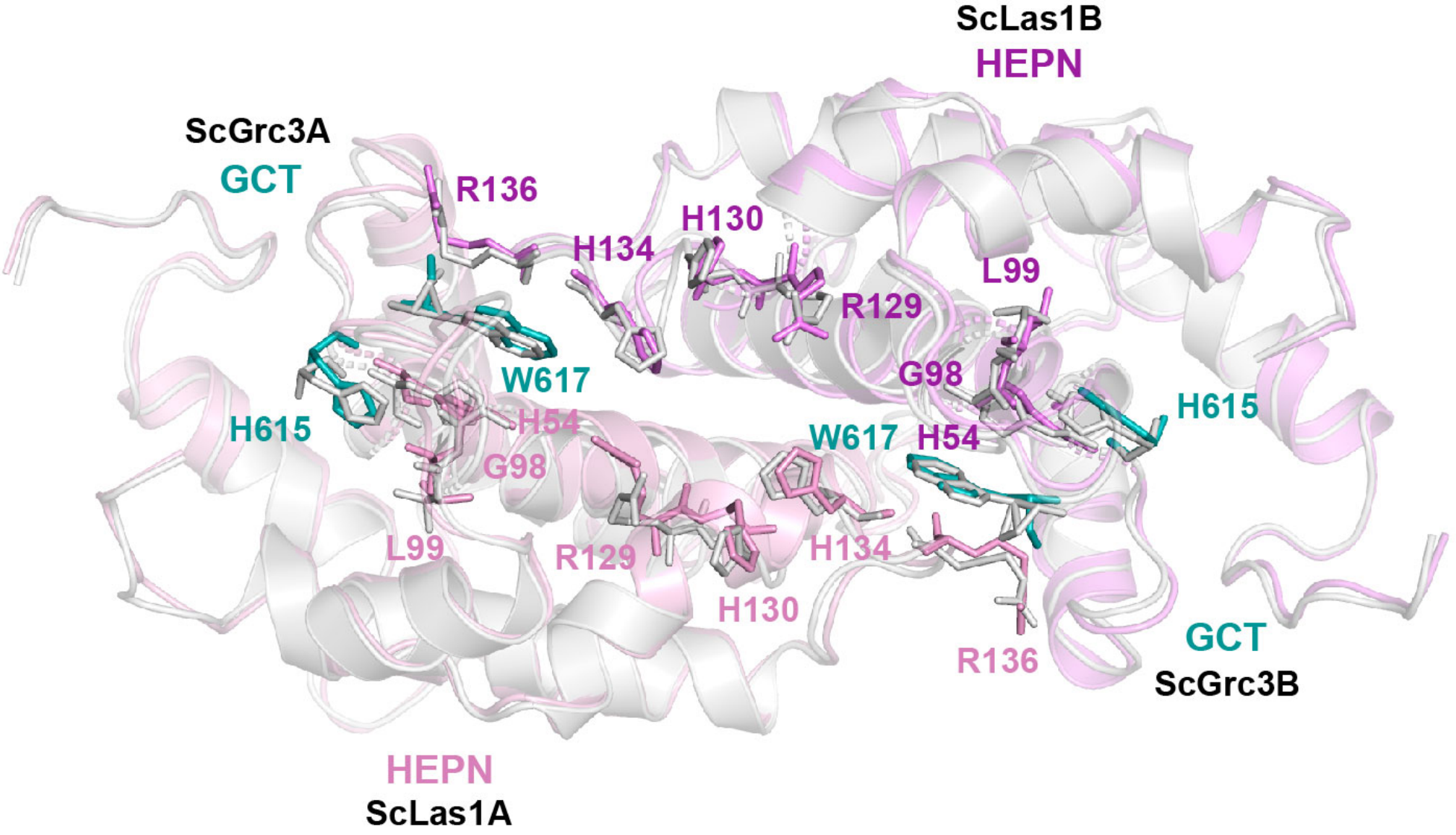

Figure 5—figure supplement 2

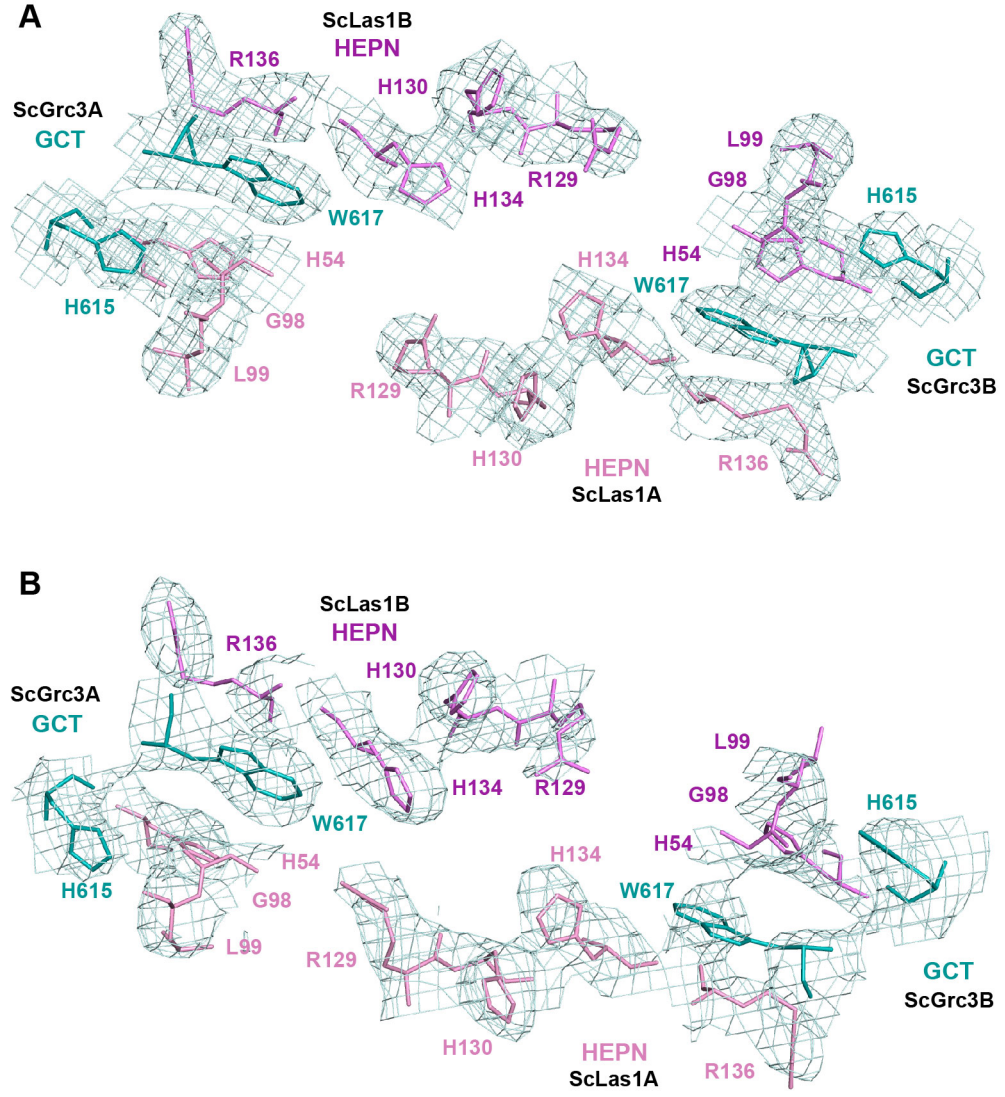

Figure 5—figure supplement 3

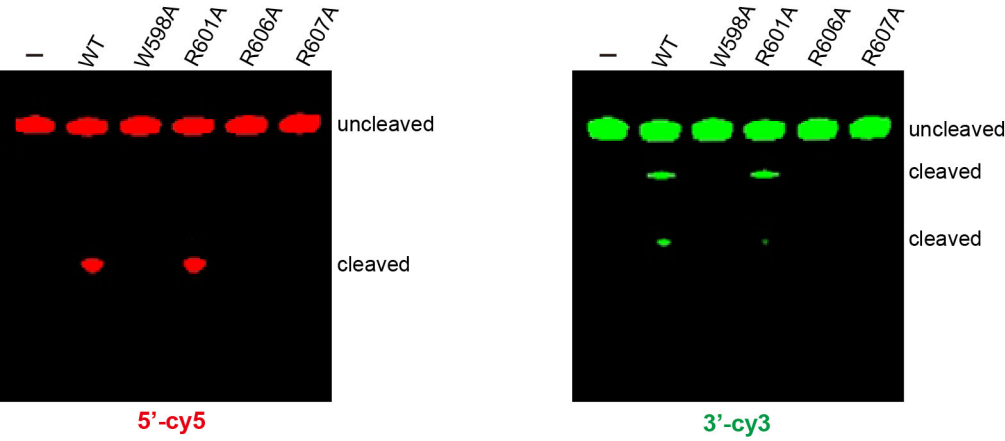

Figure 5—figure supplement 4

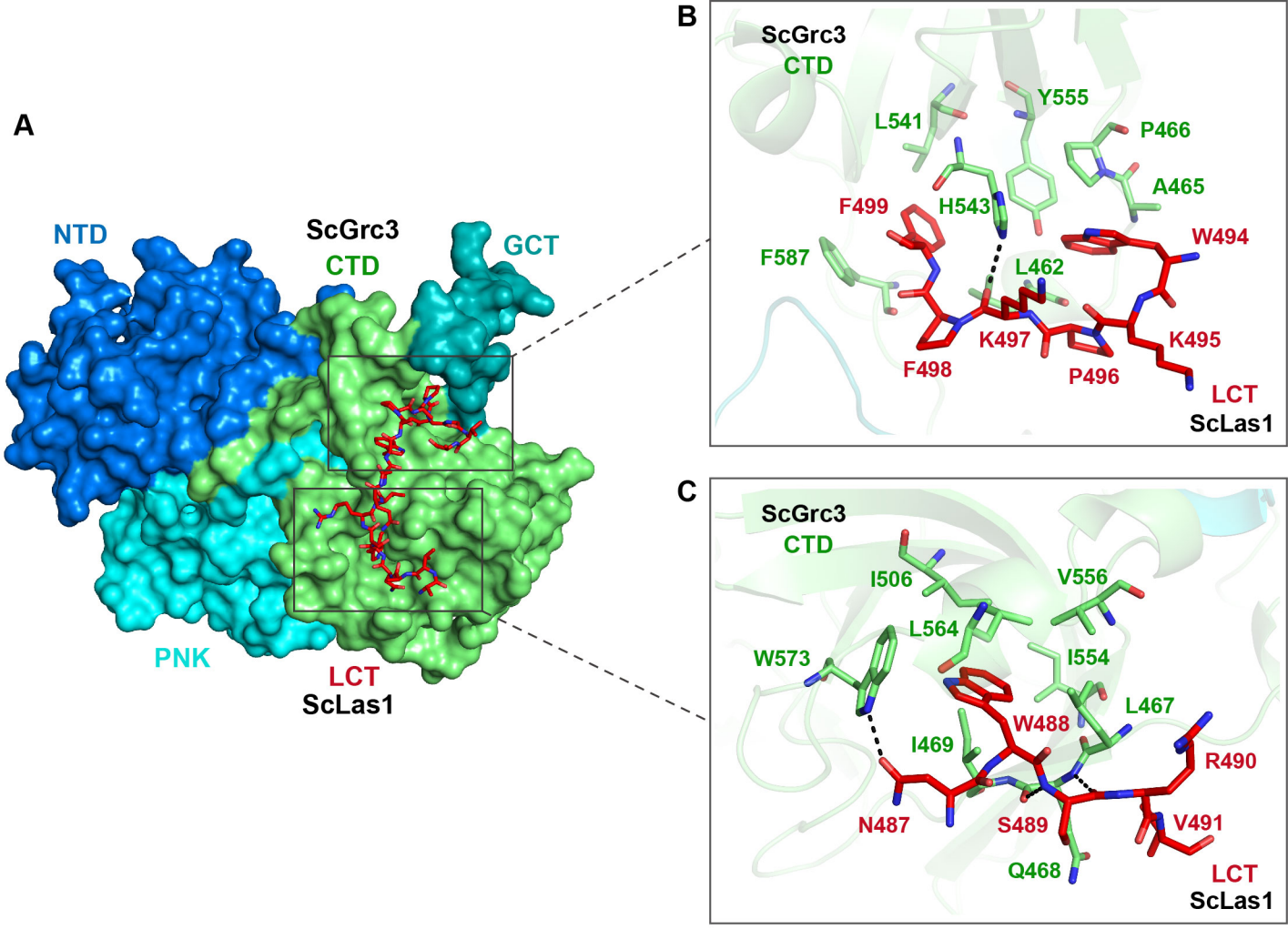
A
NTD
ScGrc3
CTD
GCT
PNK
LCT
ScLas1
B
ScGrc3
CTD
L541
Y555
P466
A465
F499
H543
W494
F587
L462
K497
K495
F498
P496
LCT
ScLas1
C
ScGrc3
CTD
I506
V556
L564
W573
I554
L467
W488
I469
R490
N487
S489
V491
Q468
LCT
ScLas1

Figure 6

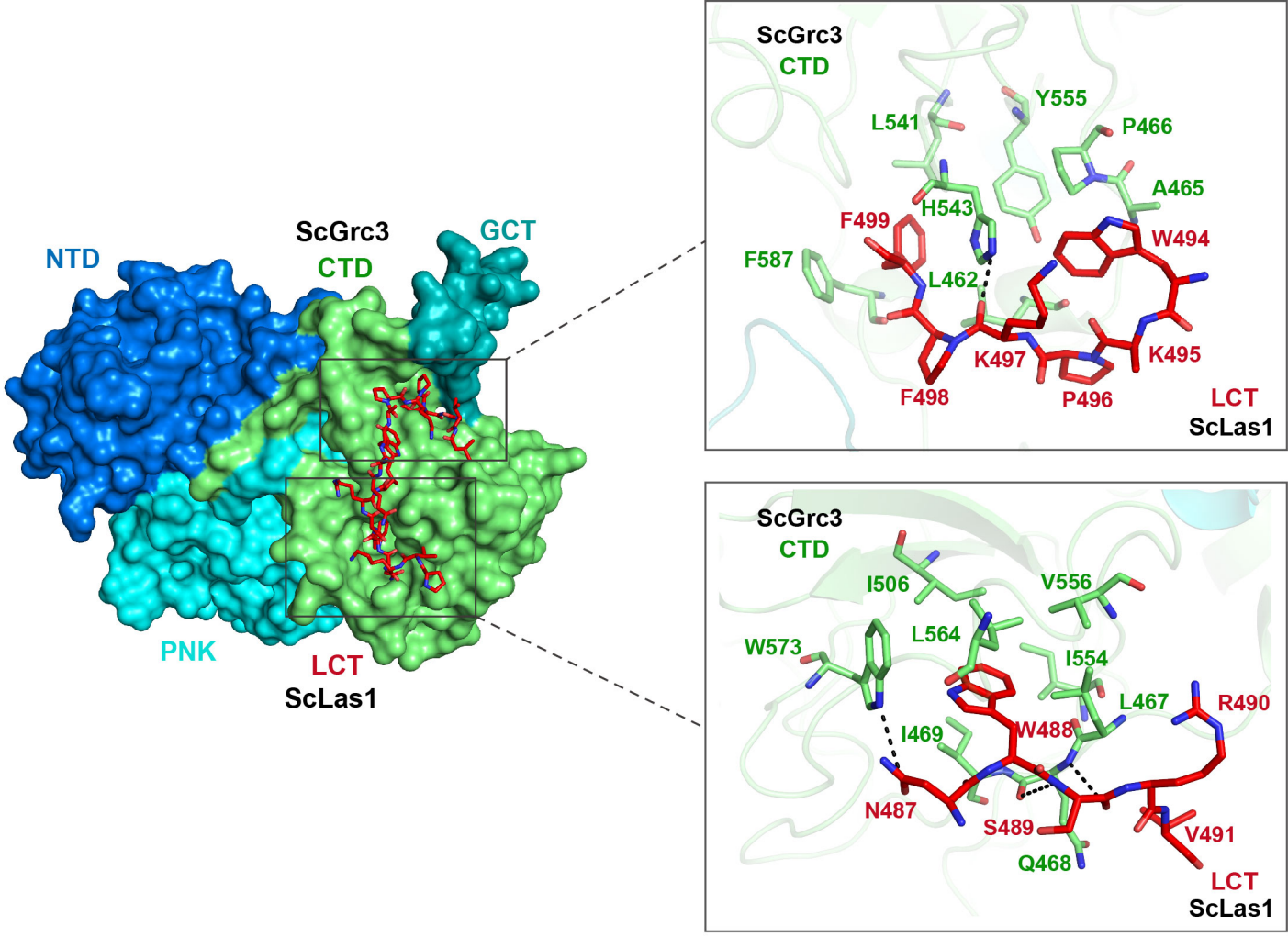

Figure 6-figure supplement 1

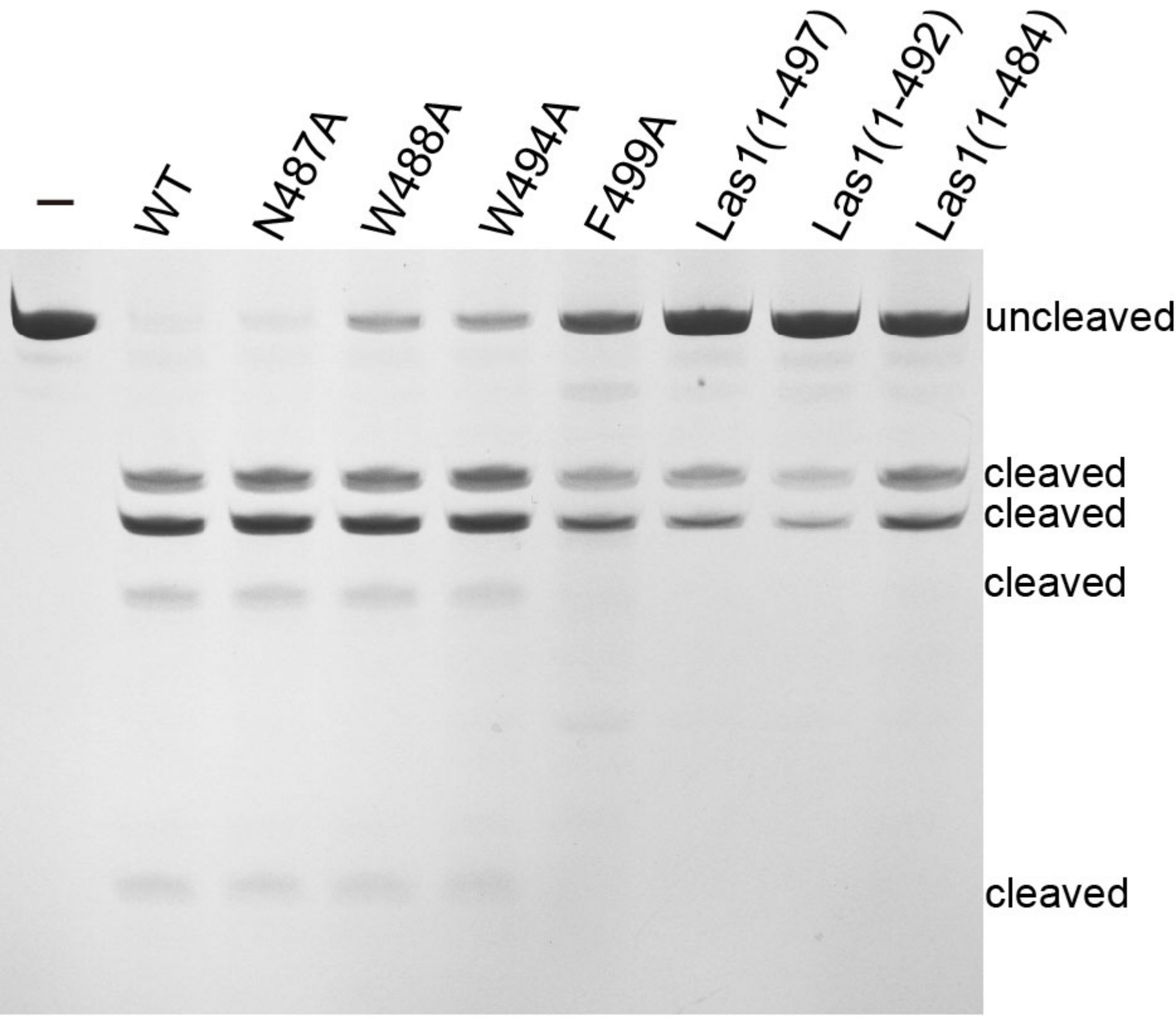

Figure 6—figure supplement 2

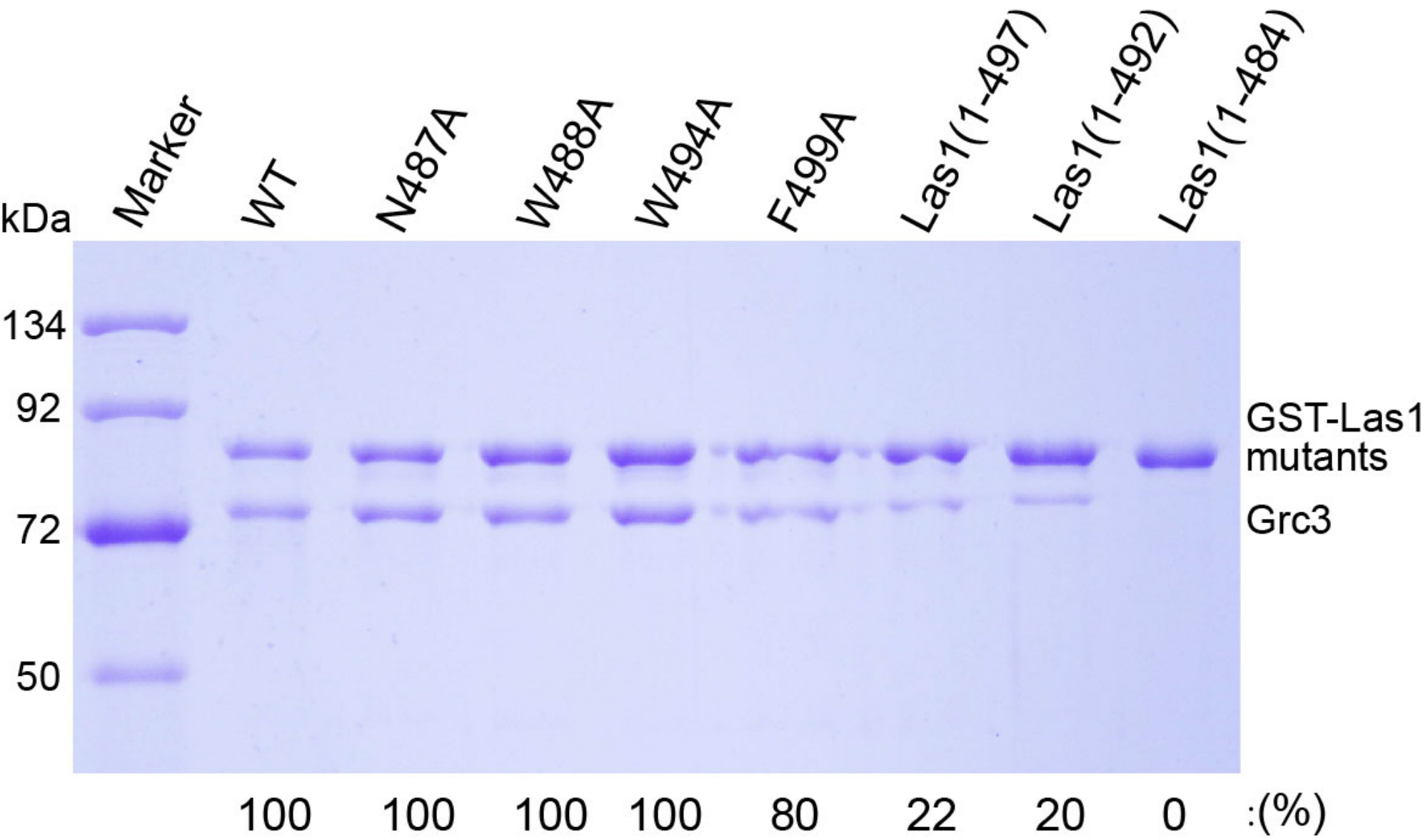

Figure 6—figure supplement 3

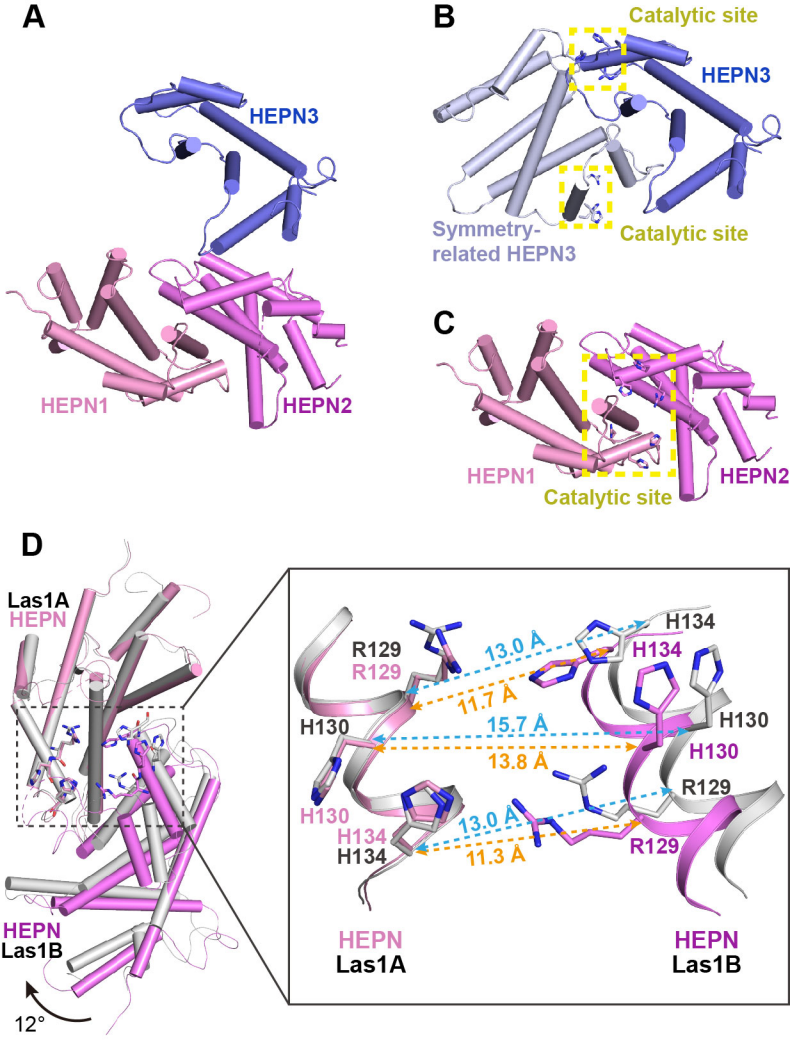
A
HEPN3
HEPN1
HEPN2
B
Catalytic site
HEPN3
Symmetry-
related HEPN3
Catalytic site
C
HEPN1
HEPN2
Catalytic site
D
Las1A
HEPN
HEPN
Las1B
12°
R129
R129
H134
H134
13.0 Å
11.7 Å
H130
15.7 Å
H130
13.8 Å
H130
R129
H130
H134
H134
13.0 Å
11.3 Å
R129
HEPN
Las1A
HEPN
Las1B

Figure 7

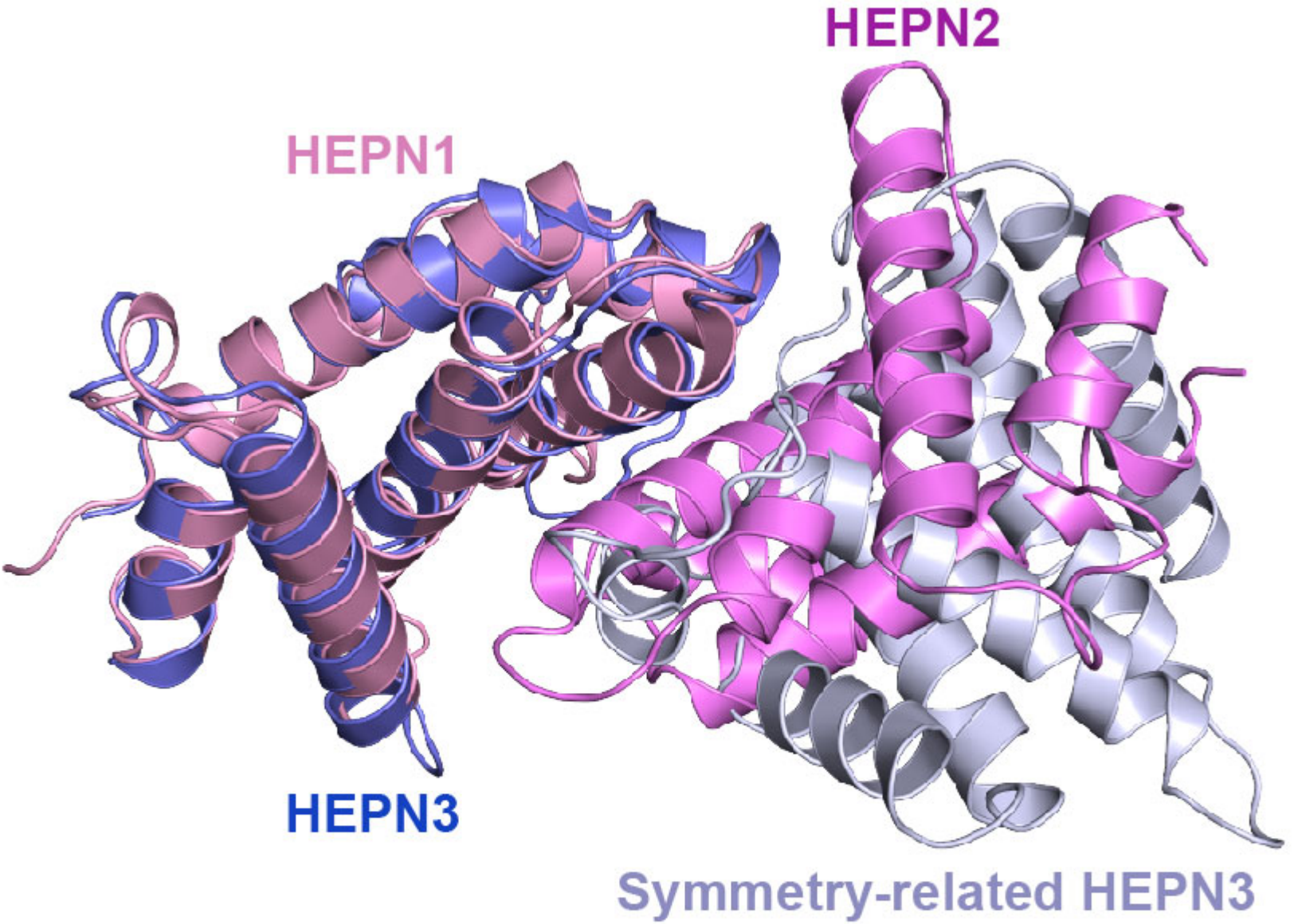

Figure 7—figure supplement 1

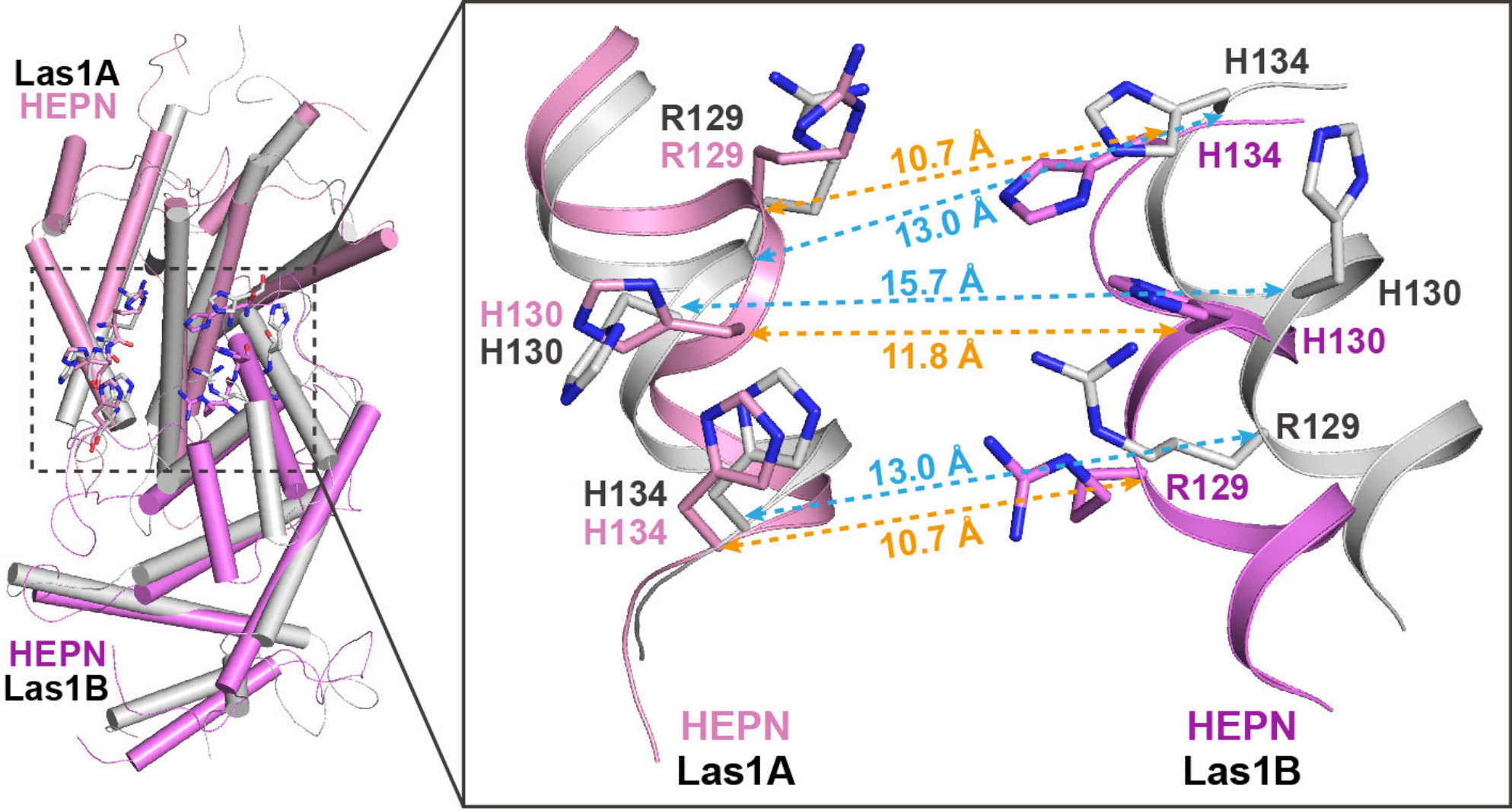

Figure 7—figure supplement 2

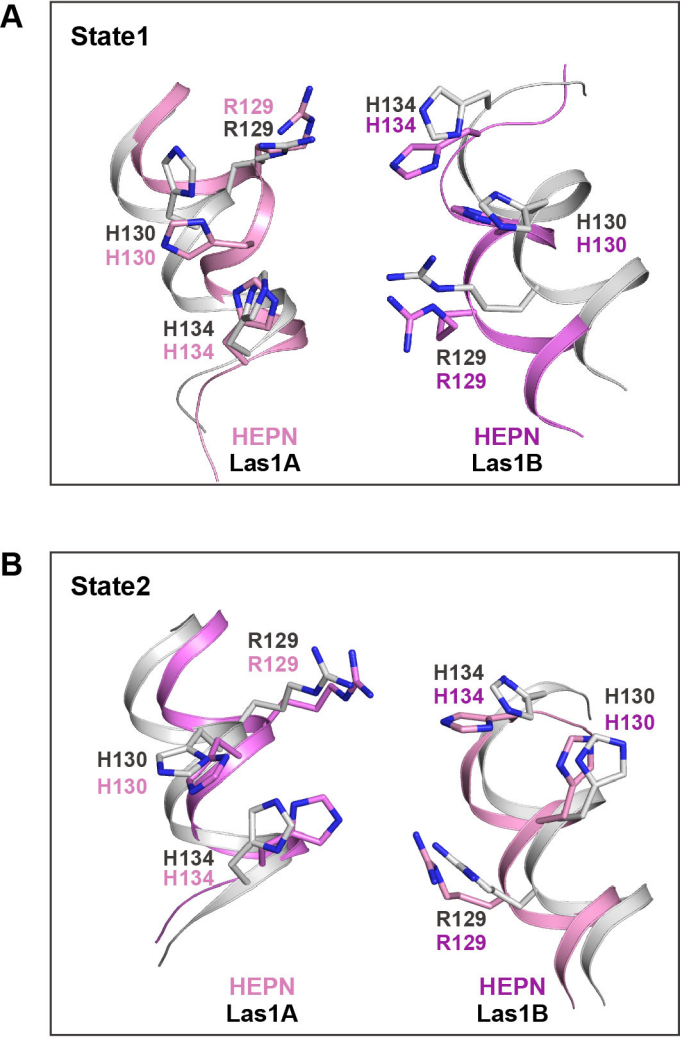

Figure 7—figure supplement 3

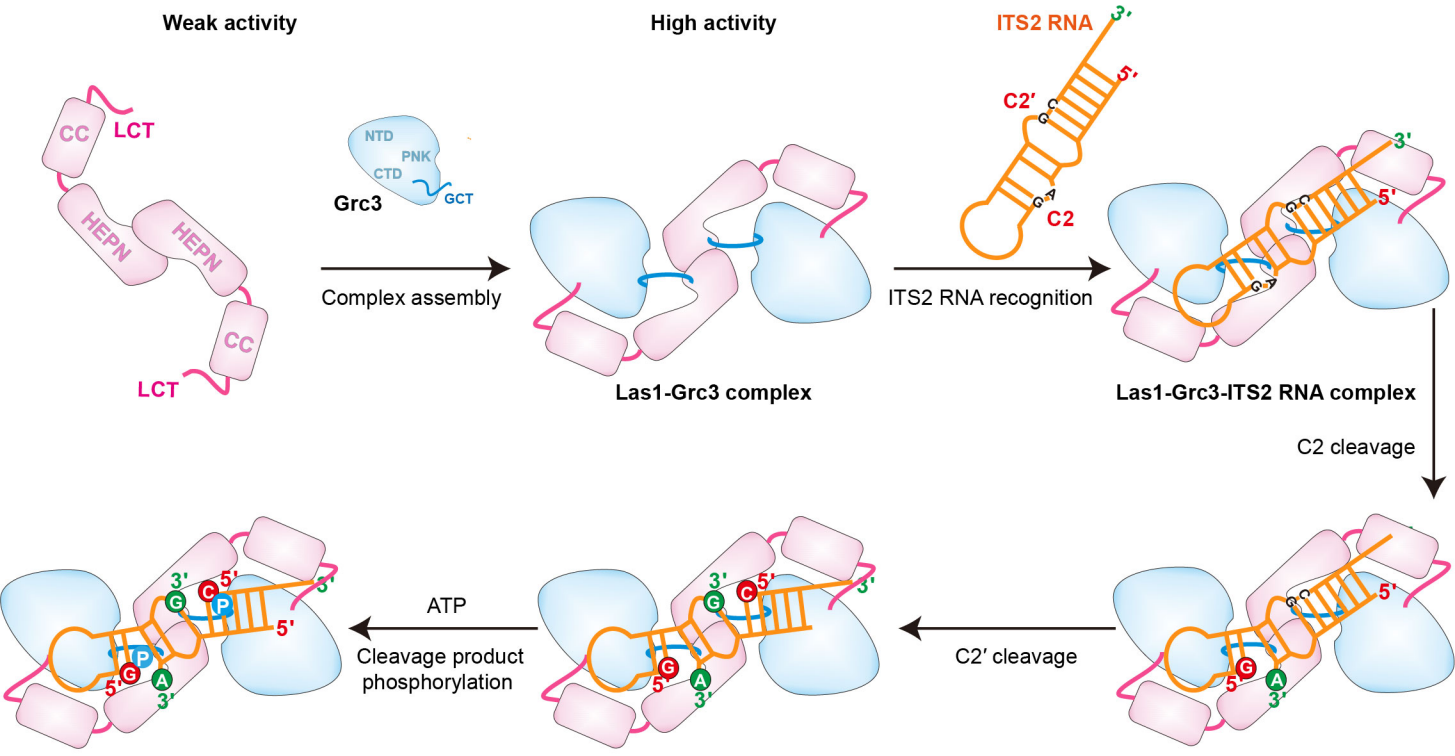
Weak activity
High activity
CC
LCT
HEPN
HEPN
CC
LCT
NTD
PNK
CTD
GCT
Grc3
Complex assembly
Las1-Grc3 complex
ITS2 RNA
3'
5'
C2'
C2
ITS2 RNA recognition
Las1-Grc3-ITS2 RNA complex
C2 cleavage
C2' cleavage
ATP
Cleavage product
phosphorylation
G
C
A
P

Figure 8

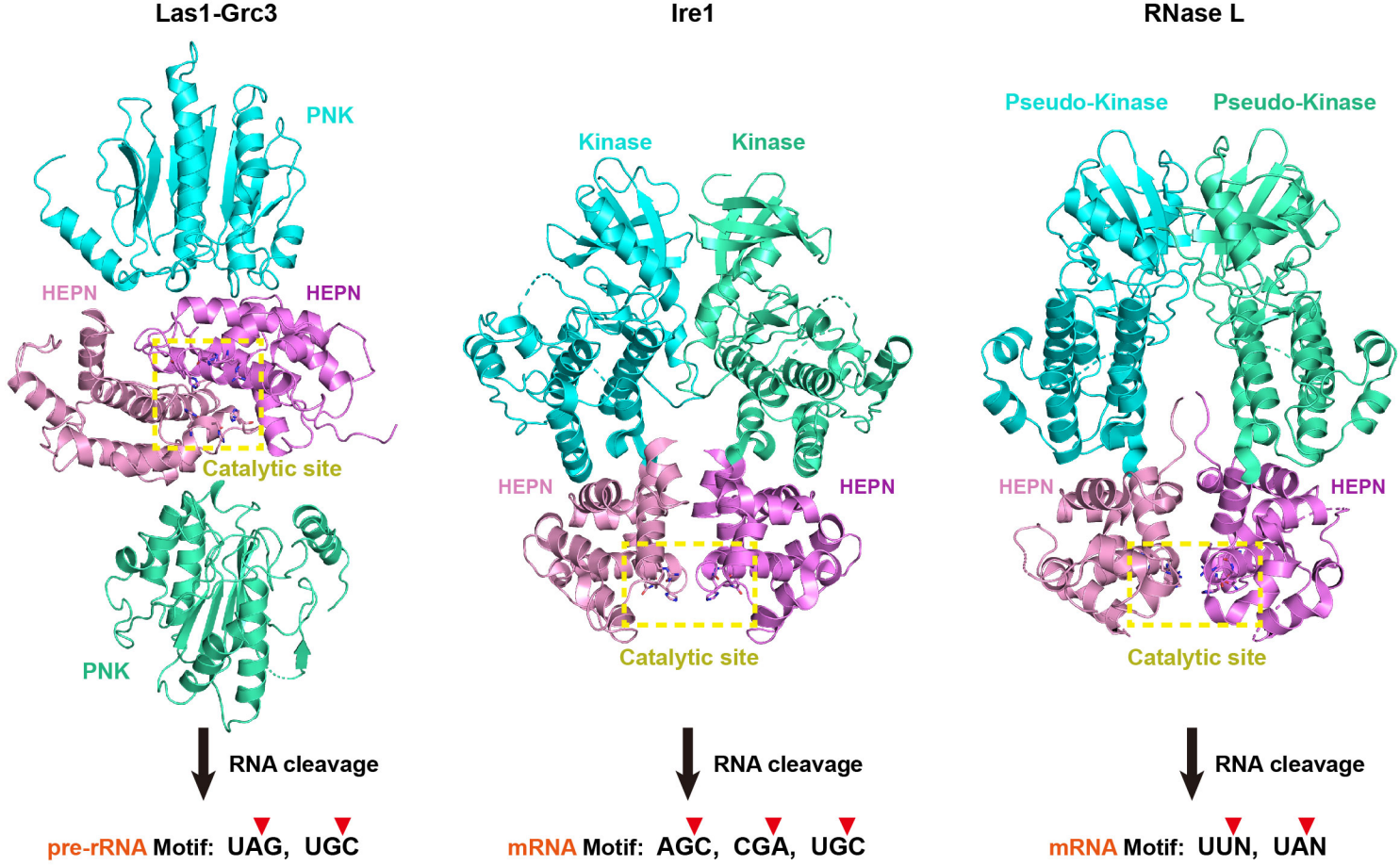

Figure 8—figure supplement 1